115

A Reliable and Efficient Two-Stream Algorithm for Spherical Radiative Transfer: Documentation of Accuracy in Realistic Layered Media

A. KYLLING and K. STAMNES
University of Alaska Fairbanks, Geophysical Institute, PO Box 757320, 903 Koyukuk Dr., Fairbanks, Alaska 99775-7320, U.S.A.

and

S.-C. TSAY
Climate and Radiation Branch, NASA/GSFC, Mail Code 913, Greenbelt, MD 20771, U.S.A.

Abstract. We present a fast and well documented two-stream algorithm for radiative transfer and particle transport in vertically inhomogeneous, layered media. The physical processes considered are internal production (emission), scattering, absorption, and Lambertian reflection at the lower boundary. The medium may be forced by internal sources as well as by parallel or uniform incidence at the top boundary. This two-stream algorithm is based on a general purpose multi-stream discrete ordinate algorithm released previously. It incorporates all the advanced features of this well-tested and unconditionally stable algorithm, and includes two new features: (i) corrections for spherical geometry, and (ii) an efficient treatment of internal sources that vary rapidly with depth. It may be used to compute fluxes, flux divergences and mean intensities (actinic fluxes) at any depth in the medium. We have used the numerical code to investigate the accuracy of the two-stream approximation in vertically inhomogeneous media. In particular, computations of photodissociation and warming/cooling rates and surface fluxes of ultraviolet and visible radiation for clear, cloudy and aerosol-loaded atmospheres are presented and compared with results from multi-stream computations. The $O_3 + h\nu \rightarrow O(^1D) + O_2$ and $O_3 + h\nu \rightarrow O(^3P) + O_2$ photodissociation rates were considered for solar zenith angles between 0.0–$70.0°$ and surface albedos in the range 0.0–1.0. For small and moderate values of the solar zenith angle and the surface albedo the error made by the two-stream approximation is generally smaller, $< 10\%$, than the combined uncertainty in cross sections and quantum yields. Surface ultraviolet and visible fluxes were calculated for the same range of solar zenith angles and surface albedos as the photodissociation rates. It was found that surface ultraviolet and visible fluxes may be calculated by the two-stream approximation with 10% error or less for solar zenith angles less than $60.0°$ and surface albedos less than 0.5. For large solar zenith angles and/or large surface albedos, conditions typical at high latitudes, the error made by the two-stream approximation may become appreciable, i.e. 20% or more for the photodissociation rates in the lower stratosphere and for ultraviolet and visible surface fluxes for large surface albedos. The two-stream approximation agrees well with multi-stream results for computation of warming/cooling rates except for layers containing cloud and aerosol particles where errors up to 10% may occur. The numerical code provides a fast, well-tested and robust two-stream radiative transfer program that can be used as a 'software tool' by aeronomers, atmospheric physicists and chemists, climate modellers, meteorologists, photobiologists and others concerned with radiation or particle transport problems. Copies of the FORTRAN77 program are available to interested users.

Key words: Radiative transfer, spherical geometry, photodissociation, photolysis, J-values, warming/cooling, clouds, aerosols, errors, two-stream, algorithm.

In spite of the profilic literature on various two-stream and related Eddington approximations, documentation is still lacking pertaining to the adequacy of this method for the computation of radiative warming/cooling and photodissociation rates and surface fluxes in vertically inhomogeneous atmospheres containing cloud and aerosol layers. Therefore, an important aspect of this paper is to provide assessments of the accuracy provided by this simple approximation for such computations under realistic atmospheric conditions.

The paper is organised as follows. In Section 2 theoretical aspects of the two-stream method are briefly discussed. Matters concerning the numerical implementation are discussed in Section 3. The accuracy of the two-stream method is thoroughly discussed in Section 4. Finally, in Section 5, a brief summary of the paper is given.

2. Theory

2.1. BASIC EQUATIONS

Knowledge of the mean intensity and fluxes is sufficient to compute photodissociation and warming/cooling rates and radiation doses. Thus, we start with the discrete ordinate approximation to the radiative transfer equation pertinent for the diffuse, azimuthally-averaged, monochromatic intensity $I(\tau, \mu)$ (cf., e.g., Chandrasekhar, 1960; Stamnes, 1986)

$$\mu\frac{\mathrm{d}I(\tau, \mu)}{\mathrm{d}\tau} = I(\tau, \mu) - S(\tau, \mu), \tag{1}$$

where the source function $S(\tau, \mu)$ at optical depth τ and polar angle $\theta = \cos^{-1}\mu$ in the two-stream approximation (hereafter referred to as TSA*) is

$$\begin{aligned} S(\tau, \mu) &= a(\tau)b(\tau, \mu)I(\tau, -\mu_1)+ \\ &+ a(\tau)[1 - b(\tau, \mu)]I(\tau, +\mu_1) + Q(\tau, \mu). \end{aligned} \tag{2}$$

Here μ_1 is the quadrature angle, $a(\tau)$ the single scattering albedo and $Q(\tau, \mu)$ the internal source. Furthermore, the backscattering coefficient

$$b(\tau, \mu) = \tfrac{1}{2}(1 - 3g(\tau)\mu\mu_1), \tag{3}$$

describes the probability that a photon upon scattering will change direction from one hemisphere to the other. The asymmetry factor $g(\tau)$ is 1.0 for complete forward scattering, −1.0 for complete backward scattering and 0.0 for isotropic scattering. Polarization is not accounted for in this model. Results provided to us by P. Stamnes (personal communication, 1993), suggest that the neglect of polarization introduces errors of 1–2% in fluxes and the mean intensity for a Rayleigh scattering atmosphere. Errors of this magnitude may be ignored in most applications which use two-stream radiative transfer models.

---

* For a clear and simple derivation of the TSA and discussion of observable phenomena which can only be explained by multiple scattering, see Bohren (1987).

1. Introduction

For a number of problems in atmospheric science, it is of paramount importance to know the radiation field for a variety of atmospheric conditions. For example, computation of atmospheric photodissociation rates requires the mean intensity (proportional to the actinic flux) as a function of wavelength and altitude. Similarly, the mean intensity (or the flux divergence) is required to compute radiative warming/cooling rates. Assessment of the biological impact of ultraviolet radiation also requires the knowledge of the incident irradiance to enable computation of the appropriate dose rate. The proper definitions of these various rates are given in Section 4.1. It is sufficient to note here that all of them require integrations over wavelength and will therefore be computer-intensive.

Due to the computational burden involved in computing these radiative quantities, it is desirable to have available fast, yet accurate, and reliable algorithms for computation of the radiation field in an atmosphere under a variety of different conditions. In particular, the effects of clouds and aerosols on atmospheric radiation must be treated in a consistent manner. It is also important to include spherical geometry in order to calculate the radiation field correctly for low solar elevations.

Numerous papers have appeared over the years on various two-stream and closely related Eddington approximations for radiative transfer calculations. Most of these papers have discussed the validity of this approximation for a single homogeneous layer. The differences between various two-stream and Eddington approximations reported in the literature can be traced to the choice of numerical quadrature (or integration over polar angle), the implementation of the boundary conditions, and the treatment of the phase function for anisotropic scattering. For a discussion of the relationship between these methods, we refer to three articles in which their relative merits are also compared and assessed: Meador and Weaver (1980). Zdunkowski *et al.* (1980), King and Harshvardhan (1986). Applications to particle transport problems are discussed in Nagy and Banks (1970), Stamnes (1981), Stamnes *et al.* (1991) and Kylling and Stamnes (1992).

In this paper, we describe a new numerical implementation of the two-stream method for solving the linear transport equation applicable to radiation transfer as well as particle transport in vertically inhomogeneous layered media. The method is based on the well-tested and widely used discrete ordinate method of Stamnes *et al.* (1988), and incorporates all the advanced features of that method. In particular, the ill-conditioning problem that occurs when two or more layers are combined is entirely eliminated. In the delta-Eddington code (Wiscombe, 1977a), this problem was dealt with by subdividing layers. No such subdividing is necessary in the present code. As was the case with the general purpose discrete ordinate code released previously, we have attempted to make this two-stream code well-documented and error-free to facilitate its safe use both in data analysis and as a component of large models.
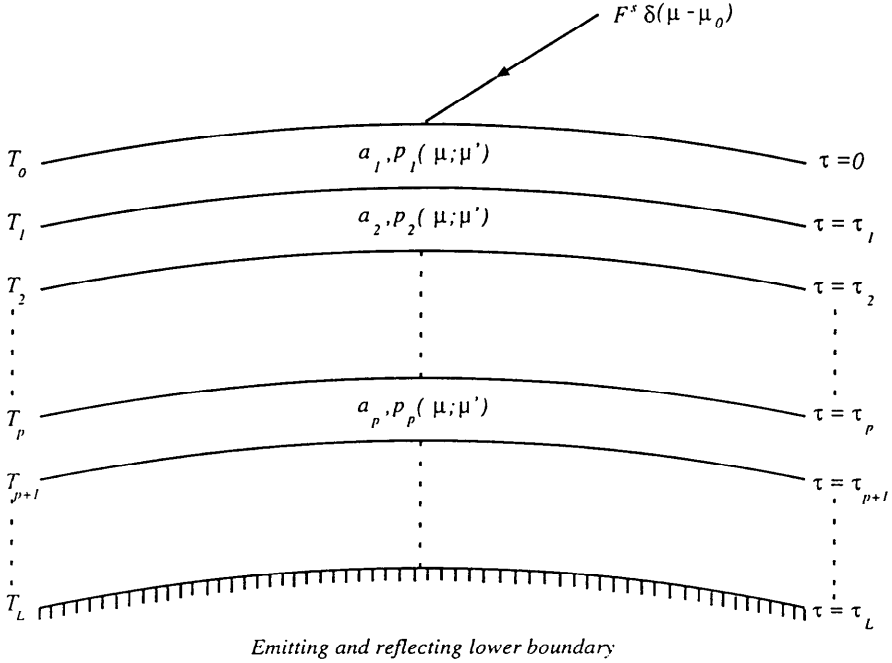
Fig. 1.   The division of the atmosphere into L adjacent homogeneous layers.

$$\overline{I(\tau)} = \frac{1}{4\pi} \int_0^{2\pi} \mathrm{d}\phi \int_{-1}^{1} \mathrm{d}\mu I(\tau, \mu, \phi) = \tfrac{1}{2}(I^+(\tau) + I^-(\tau)). \tag{10}$$

Integration of Equation (1) over 4π steradians yields the following exact relation

$$\frac{\mathrm{d}F(\tau)}{\mathrm{d}\tau} = 4\pi(1 - a)[\overline{I(\tau)} - Q(\tau)], \tag{11}$$

where the net flux $F(\tau) = F^+(\tau) - F^-(\tau)$. For thermal sources we get

$$\frac{\mathrm{d}F(\tau)}{\mathrm{d}\tau} = 4\pi(1 - a)(\overline{I(\tau)} - B[T(\tau)]). \tag{12}$$

In the numerical code the flux divergence is calculated from the mean intensity by Equation (12) and not by differencing fluxes. Note that in Equations (11) and (12) the mean intensity refers to the sum of diffuse and direct radiation.

3. Numerical Implementation and Verification

3.1. δ–M TRANSFORMATION

To accommodate strongly forward-peaked phase functions we use the δ–M transformation (Joseph et al., 1976; Wiscombe, 1977b) in which the forward scattering

For atmospheric radiation problems the internal source $Q(\tau, \mu)$ is given by

$$Q(\tau, \mu) = Q^{\text{thermal}}(\tau) + Q^{\text{beam}}(\tau, \mu), \tag{4}$$

where

$$Q^{\text{thermal}}(\tau) = [1 - a(\tau)]B[T(\tau)], \tag{5}$$

$$Q^{\text{beam}}(\tau, \mu) = \frac{a(\tau)}{4\pi} F^s (1 - 3g(\tau)\mu\mu_0) e^{-\text{ch}(\tau, \mu_0)}. \tag{6}$$

Here $B[T(\tau)]$ is the Planck function at the local temperature T and $\text{ch}(\tau, \mu_0)$ the Chapman function describing the optical path through a spherical atmosphere. In plane parallel (slab) geometry, the Chapman function is simply τ/μ_0, i.e., the slant optical path. In a curved atmosphere the slant path becomes less than in slab geometry (Section 4.4 and Appendix B). Equation (6) is the solar pseudo-source arising from the usual diffuse-direct intensity splitting (recall that $I(\tau, \mu)$ in Equation (1) describes the diffuse intensity only). Thus, $\mu_0 F^s$ is the vertical flux resulting from parallel beam radiation incident at the top boundary in direction $\theta_0 = \cos^{-1}\mu_0$.

When evaluated at the quadrature points, Equation (1) leads to two coupled differential equations. Since the single-scattering albedo $a(\tau)$ and the phase function $p(\tau, \cos\Theta)$ are functions of position τ in a vertically inhomogeneous medium, no analytic solutions exist for these two coupled differential equations. To obtain analytic solutions, the medium is divided into L adjacent homogeneous layers in which the single scattering albedo and the asymmetry factor are taken to be constant within each layer (but are allowed to vary from layer to layer, as illustrated in Figure 1), and the internal source is approximated by an exponential times linear function in τ (Appendix A). Thus, it is sufficient to consider a single homogeneous layer for which $\tau_{p-1} < \tau < \tau_p$. Evaluating Equation (1) at the quadrature points (μ_1 and $\mu_{-1} = -\mu_1$) we obtain the usual two-stream approximation (TSA) for any layer p in Figure 1

$$\mu_1 \frac{dI^+}{d\tau} = I^+ - a(1 - b)I^+ - abI^- - Q^+(\tau), \tag{7}$$

$$-\mu_1 \frac{dI^-}{d\tau} = I^- - a(1 - b)I^- - abI^+ - Q^-(\tau), \tag{8}$$

where $a = a(\tau_p)$ and $b = b(\tau_p)$. The solution of Equations (7)–(8) together with appropriate boundary conditions is outlined in Appendix A.

2.2. FLUXES, MEAN INTENSITY (ACTINIC FLUX) AND FLUX DIVERGENCE

Upward and downward fluxes and mean intensities are readily calculated in the TSA

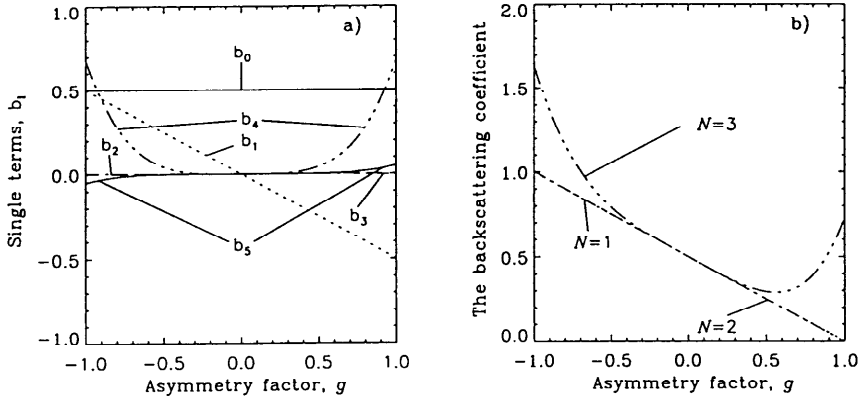$$F^\pm(\tau) = \int_0^{2\pi} d\phi \int_0^1 d\mu \mu I(\tau, \pm\mu, \phi) = 2\pi\mu_1 I^\pm(\tau), \tag{9}$$

Fig. 2. In (a) is shown the different b_l terms in the expansion of the backscattering coefficient, Equation (13). The different backscattering coefficients obtained for different choices of N are shown in (b). Note that the backscattering coefficients for $N = 1$ and $N = 2$ are indistinguishable.

negligible (Figure 2). The fourth term involving $P_4(\mu_1)$ contributes for $|g| > 0.5$ if we use a Heyney–Greenstein phase function. However, if the δ–M transformation is invoked, (Section 3.1), then $0 \leq g' \leq 0.5$ for the Heyney–Greenstein phase function. Finally, the fifth term contributes negligible for all values of g. Hence, in the TSA it is sufficient to include only the two first terms in the expansion of the backscattering coefficient (cf. Equations (3) and (6)).

3.3. QUADRATURE RULE

Possible choices for the quadrature rule in the two stream approximation include Gaussian full-range quadrature based on the interval $[-1, 1]$ or half-range (double-Gaussian) quadrature based on the ranges $[-1, 0]$ and $[0, 1]$ separately. For general multi-stream algorithms it is preferable to use double Gaussian quadrature as discussed by Stamnes *et al.* (1988). However, in the two stream approximation double Gaussian quadrature ($\mu_1 = 0.5$) gives an unphysical backscattering coefficient $b = 1/8$ for $g = 1$. The choice $\mu_1 = 1/\sqrt{3}$ (full-range Gaussian quadrature) gives the physically correct value $b = 0$. We have computed both mean intensities and fluxes, (Tables I–V), with μ_1 equal both 1/2 and $1/\sqrt{3}$. For a beam source, the quadrature angle $\mu_1 = 1/\sqrt{3}$ gives the overall best results for quantities integrated over both hemispheres, such as the mean intensity and the flux divergence, as well as for quantities integrated over single hemispheres, e.g. upward and downward fluxes. However, for thermal sources $\mu_1 = 1/2$ gives the best overall results. Hence, we recommend the use of $\mu_1 = 1/\sqrt{3}$ for beam sources and $\mu_1 = 1/2$ for thermal sources.

For a beam source, Meador and Weaver (1980) stated that '$\mu_1 = 1/\sqrt{3}$ *is not the appropriate choice for ensuring accuracy to the maximum polynomial degree for*

peak is approximated by a δ-function while the remainder is expanded in Legendre polynomials as usual. This leads to the replacement of $d\tau$ with $d\tau' = (1 - af)d\tau$, g with $g' = (g - f)/(1 - f)$, a with $a' = (1 - f)a/(1 - af)$, and $Q^\pm(\tau, \mu)$ with $Q'^\pm(\tau, \mu) = Q^\pm(\tau, \mu)/(1 - f)$ in the transport equation. In the TSA we choose the truncated fraction f of the phase function to be g^2 which is consistent with a two-term expansion of the phase function in Legendre polynomials and assuming that the angular scattering can be adequately approximatcd by a Henyey–Greenstein phase function (Joseph *et al.*, 1976). The great advantage of the δ–M transformation is that these scaling changes incurred by the truncation of the forward-scattering peak of the phase function leaves the mathematical form of the transport equation unchanged. Thus, the δ–M transformation merely makes the scattering appear more isotropic, and whatever approaches (including the TSA) available to solve the unscaled equation can be readily applied to solve the scaled equation. For strongly forward-peaked scattering the solution of the scaled equation, however, yields far more accurate results than the solution of the unscaled equation. The computer code has an option for turning the δ–M transformation on and off as desired.

3.2. PHASE FUNCTION EXPANSION

Thc complete expression for the backscattering coefficient is

$$
\begin{aligned}
b(\tau, \mu) &= \tfrac{1}{2} \int_0^1 d\mu' p(-\mu, \mu') \\
&= \tfrac{1}{2} \sum_{l=0}^{2N-1} (-1)^l (2l + 1) \chi_l P_l(\mu) \int_0^1 d\mu' P_l(\mu') \\
&\equiv \sum_{l=0}^{2N-1} b_l(\tau, \mu).
\end{aligned}
\tag{13}
$$

The angular scattering is described by the phase function $p(\tau, \cos\Theta)$; Θ is the scattering angle, and $p(-\mu, \mu')$ is the azimuthally-averaged phase function. The moments of the phase function are given by

$$
\chi_l = \tfrac{1}{2} \int_{-1}^{1} d\mu' p(\mu, \mu') P_l(\mu').
\tag{14}
$$

The first moment of the phase function is usually referred to as the asymmetry factor $\chi_l \equiv g$.

In the TSA method only the first two terms ($n = 1$ in Equation (13)) in the phase function expansion are normally used. To justify the use of $N = 1$ in Equation (13) we note the following. For a quadrature angle $\mu_1 = 1/\sqrt{3}$, which is a much used choice in the TSA corresponding to the use of full-range Gaussian quadrature, $P_2(\mu_1) = 0$.[*] Thus, there is no contribution from the second term in Equation (13). Furthermore, the contribution from the third term in Equation (13) is

---

[*] The first few Legendre polynomials are $P_0(\mu) = 1$, $P_1(\mu) = \mu$, $P_2(\mu) = \tfrac{1}{2}(3\mu^2 - 1)$, $P_3(\mu) = \tfrac{1}{2}(5\mu^3 - 3\mu)$, $P_4(\mu) = \tfrac{1}{8}(35\mu^4 - 30\mu^2 + 3)$, $P_5(\mu) = \tfrac{1}{8}(63\mu^5 - 70\mu^3 + 15\mu)$.

TABLE II. Six layers results for the net flux, $F_{net} = F^+ - F^-$, and the flux divergence, $F_{div} = F_{net}^{layer, i+1} - F_{net}^{layer, i}$. The first value for each τ-level is exact, the second the Twostr results, and in parenthesis is the percent different. Cases and τ are defined in Table I. The surface albedo $A_g = 0.0$ for all five cases. The exact values are from Wiscombe (1977a) and Lenoble (1985), while Twostr refers to the present method

τ level	Case 1		Case 2		Case 3		Case 4		Case 5	
	F_{net}	F_{div}	F_{net}	F_{div}	F_{net}	F_{div}	F_{net}	F_{div}	F_{net}	F_{div}
$\tau = 0$	2.9680	0.0000	3.0180	0.0170	1.3450	0.0190	0.4800	0.0000	2.7760	1.1610
$\tau = 0$	2.9675	0.0000	3.0089	0.0169	1.3496	0.0174	0.4580	0.0003	2.7658	1.1605
$\tau = 0$	(0.0)	(0.0)	(0.3)	(0.7)	(−0.3)	(8.4)	(4.6)	(0.0)	(0.4)	(0.0)
$\tau/20$	2.9680	0.0000	3.0010	0.0180	1.3260	0.0200	0.4800	0.0000	1.6050	0.7750
$\tau/20$	2.9675	0.0000	2.9920	0.0169	1.3323	0.0169	0.4578	0.0003	1.6053	0.7832
$\tau/20$	(0.0)	(0.0)	(0.3)	(6.1)	(−0.5)	(15.3)	(4.6)	(0.0)	(0.0)	(−1.1)
$\tau/10$	2.9680	0.0000	2.9830	0.0350	1.3060	0.0400	0.4800	0.0000	0.8300	0.6340
$\tau/10$	2.9675	0.0000	2.9751	0.0338	1.3153	0.0326	0.4574	0.0007	0.8221	0.6393
$\tau/10$	(0.0)	(0.0)	(0.3)	(3.4)	(−0.7)	(18.5)	(4.7)	(0.0)	(1.0)	(−0.8)
$\tau/5$	2.9680	0.0000	2.9480	0.1060	1.2660	0.1090	0.4800	0.0000	0.1960	0.1940
$\tau/5$	2.9675	0.0000	2.9413	0.1010	1.2827	0.0880	0.4567	0.0018	0.1827	0.1814
$\tau/5$	(0.0)	(0.0)	(0.2)	(4.7)	(−1.3)	(19.2)	(4.8)	(0.0)	(6.8)	(6.5)
$\tau/2$	2.9680	0.0000	2.8420	0.0870	1.1570	0.0780	0.4800	0.0000	0.0022	0.0021
$\tau/2$	2.9675	0.0000	2.8402	0.0826	1.1947	0.0632	0.4549	0.0009	0.0013	0.0013
$\tau/2$	(0.0)	(0.0)	(0.1)	(5.0)	(−3.3)	(18.9)	(5.2)	(0.0)	(40.2)	(38.3)
$3\tau/4$	2.9680	0.0000	2.7550	0.0840	1.0790	0.0630	0.4800	0.0000	0.0001	0.0001
$3\tau/4$	2.9675	0.0000	2.7576	0.0802	1.1314	0.0549	0.4540	0.0004	0.0000	0.0000
$3\tau/4$	(0.0)	(0.0)	(−0.1)	(4.6)	(−4.9)	(12.8)	(5.4)	(0.0)	(81.0)	(0.0)
τ	2.9680	0.0000	2.6710	0.0000	1.0160	0.0000	0.4800	0.0000	0.0000	0.0000
τ	2.9675	0.0000	2.6775	0.0000	1.0765	0.0000	0.4536	0.0000	0.0000	0.0000
τ	(0.0)	(0.0)	(−0.2)	(0.0)	(−6.0)	(0.0)	(5.5)	(0.0)	(0.0)	(0.0)

TABLE I. Single layer results for the diffuse upward and downward fluxes at the top and bottom of the layer. The surface albedo $A_g = 0.0$ for all five cases. The exact values are from Wiscombe (1977a) and Lenoble (1985), while Twostr refers to the present method

Case	μ_0	τ_{tot}	a	g	$F^+(0)$		Error	$F^-(\tau_{tot})$		Error
					Exact	Twostr	[%]	Exact	Twostr	[%]
1	1.000	1.00	1.0000	0.7940	0.173	0.174	0.65	1.813	1.812	−0.07
2	1.000	1.00	0.9000	0.7940	0.124	0.133	7.03	1.516	1.522	0.38
3	0.500	1.00	0.9000	0.7940	0.226	0.221	−2.14	0.803	0.864	7.59
4	1.000	64.00	1.0000	0.8480	2.662	2.683	0.81	0.480	0.454	−5.50
5	1.000	64.00	0.9000	0.8480	0.376	0.376	−0.05	0.000	0.000	0.00

the integrands in the integrals with limit 0 and 1'. The reason for this statement is that for thin atmospheres negative reflectances are obtained when $g > 1/(\sqrt{3}\mu_0)$, (cf. Equation (6)). However, if the δ–M transformation is invoked then $|g'| < 0.5$ for Heyney–Greenstein phase functions implying that $g' < 1/(\sqrt{3}\mu_0)$ is always true. Hence, negative reflectances are not a problem with the quadrature method when it is combined with the δ–M transformation (see also King and Harshvarhan 1986, Joseph *et al.*, 1976).

In the classification system of Meador and Weaver (1980) the present two-stream method is a quadrature method with $\gamma_1 = (\sqrt{3}/2)(2 - a(1 + g))$, $\gamma_2 = (\sqrt{3}a/2)(1 - g)$ and $\gamma_3 = (1/2)(1 - \sqrt{3}g\mu_0)$ for $\mu_1 = 1/\sqrt{3}$ when the δ–M transformation is not invoked. With the δ–M transformation it is similar to the δ-two-stream method (or δ-discrete ordinate) (King and Harshvardhan, 1986; Schaller, 1979).

3.4. AVOIDANCE OF SINGULARITIES

The inhomogeneous solution to Equations (7)–(8) contains exponentials with arguments proportional to a constant α (see Appendix). As noted by Kylling and Stamnes (1992) values of α (cf. Equation (22)) close or equal to any of the eigenvalues k require special consideration. The reason is that the particular solution due to an internal source becomes infinite as the denominator in Equations (24)–(25) approaches zero. To handle this case numerically we use so-called 'dithering' which consists of keeping α away from k by a prescribed small amount which depends on machine architecture. For single precision calculations on a 32 bit machine satisfactory results are obtained by making α deviate from k by two percent.

3.5. COMPARISON WITH EXACT RESULTS

The accuracy of both the beam source and the thermal source solutions must be tested. For the beam source we use the same tests as those utilised by Toon *et al.* (1989) to compare their two-stream radiation model with exact results (cf.

TABLE V. Single layer results for thermal radiation for different optical depths, single scattering albedos and asymmetry factors. The temperature varies linearly between 200.0 K at the top and 300.0 K at the bottom of the layer. The Planck function is integrated over the interval 300.0–800.0 cm^{-1}. The surface temperature is 0.0 K. The exact results are from Kylling and Stamnes (1992) and from 16-stream calculations by the DISORT algorithm

τ_{tot}	a	g	$F^+(0)$		Error [%]	$F^-(\tau_{tot})$		Error [%]	$F_{net}(0) - F_{net}(\tau_{tot})$		Error [%]
			Exact	Twostr		Exact	Twostr		Exact	Twostr	
0.10	0.10	0.05	19.271	20.962	8.78	20.570	21.845	6.20	−39.839	−42.808	7.45
0.10	0.95	0.75	1.264	1.284	1.61	1.282	1.302	1.55	−2.575	−2.586	0.43
1.00	0.10	0.05	80.164	87.446	9.08	115.189	127.844	10.99	−195.348	−215.290	10.21
1.00	0.95	0.75	11.317	11.640	2.85	12.816	12.987	1.33	−24.135	−24.627	2.04
10.00	0.10	0.05	63.725	61.563	−3.39	202.096	204.079	0.98	−265.788	−265.642	−0.05
10.00	0.95	0.75	53.001	48.498	−8.50	83.633	82.340	−1.55	−136.632	−130.838	−4.24
100.0	0.10	0.05	56.541	55.972	−1.01	214.720	213.967	−0.35	−270.983	−269.939	−0.39
100.00	0.95	0.75	39.423	34.352	−12.86	132.715	118.717	−10.55	−172.113	−153.069	−11.07

TABLE III. Single layer results for the mean intensity for conservative Rayleigh scattering ($a = 1$, $g = 0$). The exact values are from Wiscombe (1977a) and Lenoble (1985), while Twostr refers to the present method

μ_0	τ	$A_g = 0.00$		Error	$A_g = 0.25$		Error	$A_g = 0.80$		Error
		Exact	Twostr	[%]	Exact	Twostr	[%]	Exact	Twostr	[%]
					$4\pi\overline{I(0)}/F^s$					
0.10	0.02	1.045	1.016	−2.8	1.089	1.061	−2.6	1.187	1.161	−2.2
0.10	0.25	1.170	1.085	−7.3	1.189	1.107	−6.9	1.239	1.165	−6.0
0.10	1.00	1.212	1.119	−7.7	1.220	1.128	−7.5	1.247	1.166	−6.5
0.40	0.02	1.047	1.017	−2.9	1.235	1.210	−2.1	1.653	1.640	−0.8
0.40	0.25	1.284	1.164	−9.3	1.402	1.296	−7.5	1.707	1.645	−3.7
0.40	1.00	1.534	1.374	−10.4	1.584	1.431	−9.7	1.778	1.650	−7.2
0.92	0.02	1.040	1.017	−2.2	1.477	1.467	−0.7	2.453	2.471	0.7
0.92	0.25	1.279	1.191	−6.9	1.597	1.542	−3.4	2.404	2.466	2.6
0.92	1.00	1.691	1.572	−7.1	1.851	1.754	−5.2	2.398	2.457	2.5
					$4\pi\overline{I(\tau)}/F^s$					
0.10	0.02	0.864	0.834	−3.4	0.912	0.881	−3.4	1.018	0.985	−3.3
0.10	0.25	0.192	0.156	−18.6	0.224	0.188	−16.1	0.307	0.271	−11.6
0.10	1.00	0.057	0.054	−4.4	0.082	0.081	−1.1	0.168	0.183	9.2
0.40	0.02	0.998	0.968	−3.0	1.203	1.168	−2.9	1.661	1.613	−2.9
0.40	0.25	0.787	0.693	−11.9	0.988	0.883	−10.6	1.502	1.382	−8.0
0.40	1.00	0.385	0.344	−10.6	0.540	0.500	−7.4	1.071	1.099	2.6
0.92	0.02	1.018	0.996	−2.2	1.495	1.461	−2.3	2.561	2.500	−2.4
0.92	0.25	1.028	0.950	−7.6	1.560	1.453	−6.9	2.928	2.776	−5.2
0.92	1.00	0.881	0.822	−6.7	1.384	1.320	−4.6	3.109	3.241	4.2

TABLE IV. Upward and downward fluxes and the flux divergence for a single layer in limit the $a = 0$ and $a = 1$. The temperature at the top of the layer is 270.0 K and 280.0 K at the bottom. It is assumed to vary linearly across the layer. The surface temperature is 0.0 K for the $a = 0$ cases and 300.0 K for the $a = 1$ case. The Planck function is integrated over the interval 0.0–10,000.0 cm^{-1}. Exact results are from 16-stream calculations by the DISORT algorithm. The asymmetry factor $g = 0.0$

τ	a	$F^+(0)$		Error	$F^-(\tau)$		Error
		Exact	Twostr	[%]	Exact	Twostr	[%]
1.0	0.0	248.2	274.2	10.5	259.1	287.0	10.8
1000.0	0.0	301.4	301.4	0.0	348.5	348.5	0.0
10.0	1.0	53.623	41.791	−22.1	405.674	417.553	2.9

τ	a	$dF(0)/d\tau$		Error	$dF(\tau)/d\tau$		Error
		Exact	Twostr	[%]	Exact	Twostr	[%]
1.0	0.0	−669.4	−656.9	−1.9	−823.4	−820.1	−0.4
1000.0	0.0	−602.6	−602.6	0.0	−697.1	−697.1	0.0
10.0	1.0	0.000	−0.013	0.0	0.000	0.004	0.0

to calculate the radiative warming/cooling rate, which for an atmosphere in local thermodynamic equilibrium is given by, cf. Equation (12),

$$\frac{\partial T}{\partial t} = -\frac{1}{C_p \rho}\frac{\partial F(z)}{\partial z} = -\frac{4\pi}{C_p \rho}\frac{d\tau}{dz}(1 - a(\tau))(\overline{I(\tau)} - B[T(\tau)]). \tag{16}$$

Here $\partial F(z)/\partial z$ is the flux divergence, C_p is the specific heat at constant pressure and ρ the air density. Furthermore, τ is the optical depth, a the single scattering albedo and $B[T(\tau)]$ the Planck function at the local temperature T. The downward flux is required to compute the dose rate and the total dose $\mathcal{D}$. The dose rate is given by

$$\frac{d\mathcal{D}}{dt} = \int_{\lambda_1}^{\lambda_2} d\lambda A(\lambda) F^-(\tau, \lambda). \tag{17}$$

Here $A(\lambda)$ is the appropriate action spectrum and the integration extends over the spectral range across which the biological effects are incurred (cf. e.g., Dahlback *et al.*, 1989). The use of downward flux in Equation (17) assumes that the radiation is received by a horizontally oriented plane surface. For some biological applications, such as exposure of small 'bodies' suspended in air or in water (e.g., phytoplankton in the ocean), it may be more appropriate to use the integrated intensity or actinic flux (i.e., 4π times the mean intensity) instead of the irradiance analogous to what is done for the photodissociation rate. Note also that Equation (17) refers to the instantaneous dose rate. The actual dose requires integration over the time of exposure.

Accurate and fast computation of photodissociation and warming/cooling rates and surface fluxes is desirable in a number of atmospheric applications. Using the present TSA code we have computed photodissociation and warming/cooling rates and surface ultraviolet and visible fluxes for vertically inhomogeneous clear, cloudy and aerosol-loaded atmospheres. After discussing the spectral resolution, the atmospheric models used and the importance of spherical geometry, we compare TSA results with accurate multi-stream computations to estimate the error incurred by using the TSA.

4.2. SPECTRAL RESOLUTION

Photodissociation, warming/cooling and dose rates, Equations (15)–(17), are computed by replacing the integral over wavelength by a sum. The wavelength range is divided into a number of intervals depending on the specific application. Madronich and Weller (1990) investigated how the gridsize influence tropospheric photodissociation rates. It was found that the grid recommended by WMO (1986) may give errors of 10% or more for some photodissociation processes (e.g. CH_2O) while for other processes the errors were negligible. To our knowledge, no such study has been made for stratospheric photodissociation rates. The WMO (1986) grid has 50 bins with 500.0 cm^{-1} gridsize in the range 175.4–307.7 nm and a 5.0 nm

Tables IV, V and VI in their paper). Results from the present two-stream model are shown in Tables I–V. (Note that there are some misprints in Table V of Toon *et al.* (1989), which have been corrected in the present Table II). Generally the errors made by the present two-stream method are similar or smaller than those reported by Toon *et al.* (1989). Since we are solving the same problem as Toon *et al.* (1989), the slightly different results between the two solution methods are due to numerical roundoff errors. We note that running these tests without invoking the $\delta-M$ transformation increases the errors dramatically for strongly asymmetric phase functions.

In Tables IV and V, we present results for the thermal source. The upward and downward fluxes and the flux divergence as computed by the present two-stream algorithm and 'exact' 16-stream results obtained by the multi-stream discrete-ordinate algorithm of Stamnes *et al.* (1988; DISORT) are shown in Table IV. The 16-stream computations are accurate to 3–4 digits and considered as 'benchmark'. The tests for $a = 0$ are 'extreme' because the TSA is known to break down in this limit (Toon *et al.*, 1989). These tests must thus be considered as worst cases. As can be seen the error is never larger than 10.8% for exiting fluxes while the error for the flux divergence is negligible. For $a = 1$ the flux is conserved, hence the flux divergence should be zero. DISORT does indeed yield $dF/d\tau = 0$, while the TSA code yields slightly non-zero values. In Table V single layer TSA results are compared with multilayer DISORT results taken from Table I of Kylling and Stamnes (1992).[*] Optical depths of $\tau = 0.1, 1.0, 10.0$ and 100.0, single scattering albedos of $a = 0.1$ and 0.95 and asymmetry factors of $g = 0.05$ and 0.75 are considered. The two-stream results differ from the multi-stream results by maximum 12.9%. These errors are attributed to the TSA and not the single layer approximation. Single layer multi-stream calculations with an exponential-linear-in-optical-depth internal source approximation show no or very little difference with multilayer results (Table I, Kylling and Stamnes, 1992).

4. Accuracy of the TSA for Realistic Applications

4.1. PHOTODISSOCIATION RATE, WARMING/COOLING RATE AND BIOLOGICALLY EFFECTIVE DOSE RATE

For the calculation of photodissociation rates

$$J(z) = 4\pi \int_0^\infty d\lambda q(\lambda)\sigma(\lambda)\overline{I(z, \lambda)}, \tag{15}$$

the mean intensity $\overline{I(z, \lambda)}$ at wavelength λ and altitude z is required in addition to the appropriate quantum yields $q(\lambda)$ and cross sections $\sigma(\lambda)$. Note that the actinic flux is $4\pi \times$ mean intensity (Madronich, 1987). The mean intensity is also required

---

[*] In the caption of Table I of Kylling and Stamnes (1992) there is a misprint. The values for a and g have been interchanged. The correct values, provided in the text of that paper, are $a = 0.95$, $g = 0.75$.
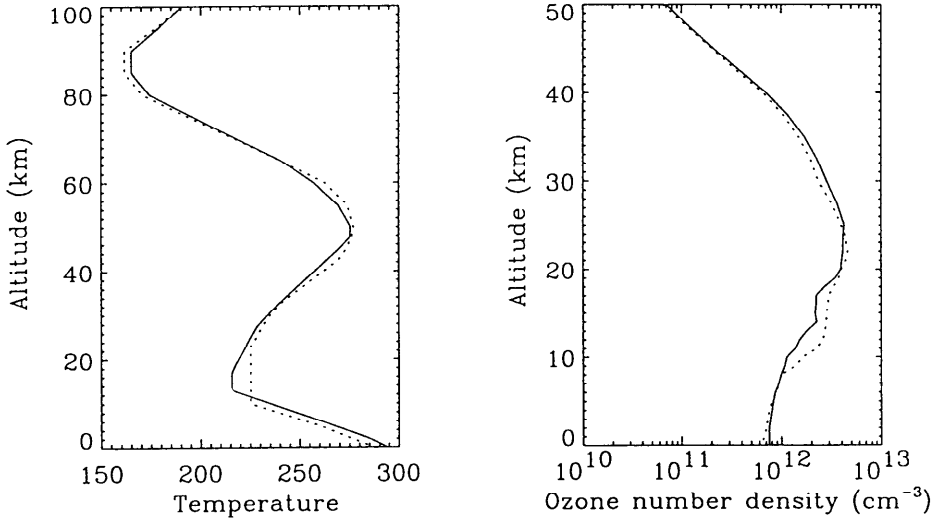
Fig. 3.   The temperature and ozone profiles for the midlatitude (solid lines) and the subarctic (dotted lines) atmospheres (Anderson *et al.*, 1987).

Also shown, are extinction coefficient profiles for moderate, high and extreme volcanic aerosol loading situations. The tropospheric aerosols are made from a variety of natural and anthropogenic chemical compounds. Their optical properties are parameterized in terms of the surface visibility. The extinction coefficient at 550.0 nm is shown for several visibilities in Figure 4.

The extreme volcanic aerosol model is representative for aerosol conditions associated with major volcanic eruptions, such as Mt. Agung (1963), El Chichon (1982) and Mount Pinatubo (1991). The optical properties of the aerosol layer change with time due to removal of aerosols and due to changes in the composition of the aerosols caused by photochemical and chemical processes. The different aerosol models shown in Figure 4 represent various stages in the evolution of the stratospheric aerosol layer after a volcanic eruption. The time evolution will vary with the magnitude, location and time of the eruption. The extreme aerosol situation implies the strongest scattering of radiation and thus leads to the largest discrepancy between the TSA and multi-stream calculations. Hence, it was adopted for the accuracy study performed in this paper. For the troposphere, we used the model with a surface visibility of 50.0 km giving a tropospheric optical depth of $\tau \sim 0.14$ at 550.0 nm. The globally averaged optical depth of tropospheric aerosols has been estimated to be $\tau \sim 0.1$ (Hansen and Lacis, 1990), which is somewhat lower than the value adopted here.

gridsize for larger wavelengths. For the calculation of photodissociation and solar warming rates we adopted the spectral resolution recommended by WMO (1986) except between 302.0 and 314.0 nm where a gridsize of 1.0 nm was used.

Dose rates are very sensitive to the rapid change in the ozone cross section between 280.0–360.0 nm. The resolution given in WMO (1986) is to coarse to yield accurate UV-B and UV-A dose rates. Hence, a 1.0 nm resolution was adopted for the calculation of dose rates.

In the terrestrial part of the spectrum the absorption cross sections vary rapidly, erratically and by several orders of magnitude within short wavenumber intervals. Hence, the integration over wavelength is a nontrivial task. It is beyond the scope of this paper to review all the different approximations methods for performing the integration over wavelength (see Goody and Yung, 1989, for a recent review). In this study the correlated-k distribution method (Lacis and Oinas, 1991) was utilized. The wavenumber region 0.0–2,000.0 cm^{-1} was divided into 10.0 cm^{-1} intervals. In each interval 50 monochromatic radiative transfer calculations were performed. Absorption by carbon dioxide, ozone and water molecules was accounted for. The procedure used to obtain the correlated-k distribution is described in Kylling (1992). We note that the correlated-k distribution method allows multiple scattering to be included. Furthermore, it accounts for the change of the absorption line shapes with pressure thus allowing the troposphere and the stratosphere to be treated in a unified manner.

4.3. ATMOSPHERIC MODELS

In order to calculate the optical depth, single scattering albedo and asymmetry factor, the composition of the atmosphere must be known. Below we describe the atmospheric models used in the present study.

4.3.1. *Trace Gas and Temperature Profiles*

Ozone, carbon dioxide, nitrogen dioxide, water vapour and temperature profiles were taken from Anderson *et al.* (1987). The ozone and temperature profiles for the midlatitude summer and subarctic summer atmospheres used in this study are shown in Figure 3. The midlatitude summer and subarctic summer atmospheres have ozone contents of 335.7 DU and 349.0 DU respectively. The models have 50 unevenly spaced grid points between 0.0–120.0 km.

4.3.2. *Aerosol Models*

Both stratospheric and tropospheric aerosols affect the radiation field. The stratospheric aerosol layer is situated between 15 and 25 km and is composed primarily of sulfuric acid (Turco *et al.*, 1982). Being mainly of volcanic origin the stratospheric aerosol layer has a high degree of natural variability. A typical profile of the extinction coefficient for background aerosol conditions is shown in Figure 4.

a $1/\mu_0$ factor (μ_0 is the cosine of the solar zenith angle) is used instead of the Chapman function in Equation (6). Plane parallel calculations thus overestimates the optical depth of the medium and underestimates the radiation field. For solar zenith angles less than 95° a 'pseudo-spherical' approximation is adequate for the calculation of fluxes and the mean intensity (see e.g. Dahlback and Stamnes, 1991). In the 'pseudo-spherical' approximation the direct beam attenuation is computed correctly using spherical geometry (cf. the Chapman function in Equation (6)); otherwise the plane-parallel assumption is retained. For solar zenith angles larger than 95° this 'pseudo-spherical' approximation becomes inadequate because it overestimates the mean intensity as discussed by Dahlback and Stamnes (1991).

Figure 5 exemplifies the importance of including spherical geometry by showing photodissociation rates for the two different ozone channels, $J(O_3)$: $O_3 + h\nu \rightarrow O_2 + O(^3P)$ and $J(O_3^*)$: $O_3 + h\nu \rightarrow O_2 + O(^1D)$, calculated in plane-parallel and spherical geometry for twilight conditions. The rightmost column shows how the rates behave when the sun is below the horizon. Neglecting spherical geometry gives $J(O_3)$ values that are an order of magnitude to low at the surface for a solar zenith angle of 89.0°, cf. panel (a) and (b) in Figure 5. The difference decreases with increasing altitude and decreasing solar zenith angle, the plane-parallel $J(O_3)$ value being a factor 2 to low at 20.0 km for $\theta_0 = 89.0°$. The very abrupt change in the J-profiles in panel (c) for solar zenith angles 90.0° is due to the absence of direct radiation below the screening height.

4.5. PHOTODISSOCIATION RATES: 2-STREAM VERSUS MULTI-STREAM RESULTS

To estimate the error made by the TSA we have computed photodissociation rates for the processes $J(O_3)$: $O_3 + h\nu \rightarrow O_2 + O(^3P)$ and $J(O_3^*)$: $O_3 + h\nu \rightarrow O_2 + O(^1D)$ by the present TSA and by the DISORT algorithm run in 16-stream mode. The 16-stream results are accurate to 3–4 digits and hence may be used as benchmarks. The two processes $J(O_3)$ and $J(O_3^*)$ have been selected both for their importance in atmospheric chemistry and for their different spectral dependence. The rates were computed for surface albedos $A_g = 0.0$, 1/3, 2/3, 1.0 and solar zenith angles $\theta_0 = 0°, 7°, 14°, \ldots, 70°$. Solar zenith angles larger than 70° were not considered as spherical effects then may become important. Spherical effects are included in the TSA but not in the standard multi-stream algorithm DISORT. Rates were computed for clear Rayleigh scattering as well as cloudy and aerosol-loaded atmospheres. Examples of the rates for the different conditions are shown in Figure 6 for a solar zenith angle of 35° and surface albedo $A_g = 0.0$. The $J(O_3)$ rate, Figure 6a, for a cloudy sky increases relative to the clear sky values above the cloud and decreases below the cloud. A similar behavior is seen for the $J(O_3^*)$ cloudy sky rate, Figure 6b. However, in the stratosphere the cloudy sky $J(O_3^*)$ rate approaches the clear sky values. The $J(O_3^*)$ channel is produced mainly by radiation with wavelength shorter than 310 nm. Relatively little of this radiation penetrates to the Earth's surface or to clouds in the lower troposphere. Hence, the
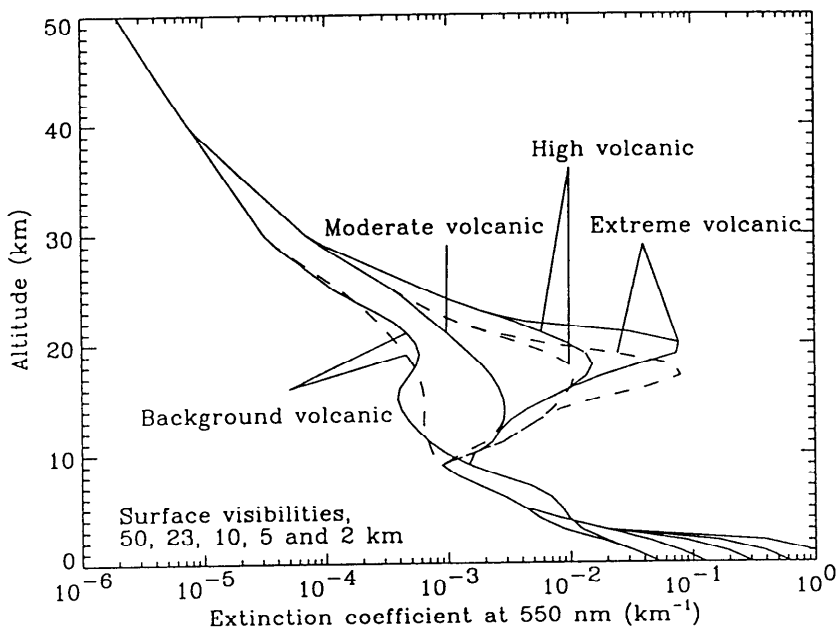
Fig. 4.   The aerosol extinction at 550 nm from the Shettle and Fenn (1989) aerosol models. The solid line represents spring–summer conditions and the dashed line fall–winter conditions.

4.3.3. *Water Cloud Model*

The optical properties of the water cloud adopted here were calculated by the parameterization scheme of Hu and Stamnes (1993). Assuming that the water droplets are spherical, they used results of detailed Mie theory calculations as a basis for developing an accurate and fast parameterization scheme. The variable parameters are the liquid water content and the effective droplet radius. These two parameters were found to be the only ones necessary to characterize the cloud radiative properties accurately (Hu and Stamnes, 1993).

For the calculations presented below, the effective droplet radius was taken to be 10.0 μm and the liquid water content 0.1 g/m^3. The cloud base is at 2.0 km and the cloud thickness is 1.0 km. The optical thickness of the cloud was about 15 at visible wavelengths.

4.4.   THE IMPORTANCE OF SPHERICAL GEOMETRY UNDER TWILIGHT CONDITIONS

For zenith angles less than 75° the atmosphere may be assumed to be plane-parallel. For larger solar zenith angles the curvature of the earth and its surrounding atmosphere decreases the pathlength that a photon travels as compared with a corresponding plane-parallel atmosphere. This is so because in plane-parallel geometry
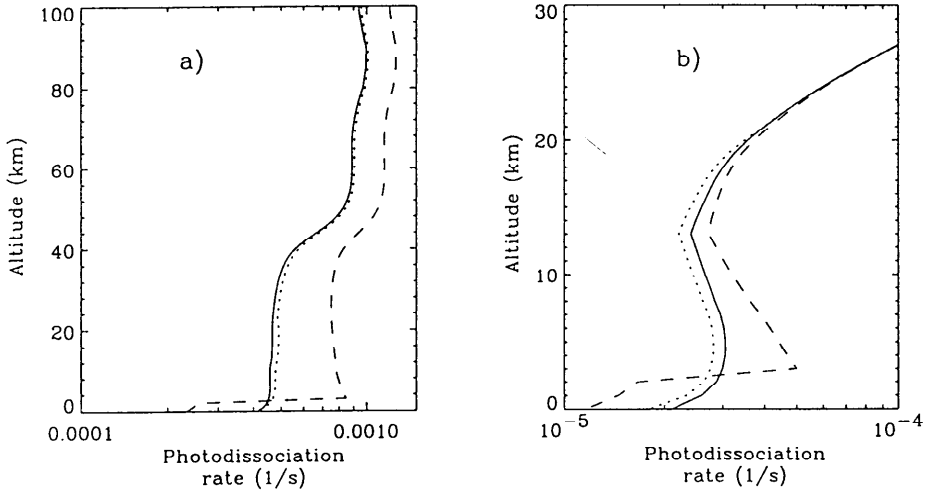
Fig. 6. The (a) $O_3 + h\nu \rightarrow O(^3P) + O_2$ and b) $O_3 + h\nu \rightarrow O(^1D) + O_2$ photodissociation rates for clear (solid line), cloudy (dashed line) and aerosol-loaded (dotted line) conditions as a function of altitude. The solar zenith angle is 35° and it is the accurate multi-stream results that are displayed. A midlatitude summer atmosphere (Anderson *et al.*, 1987) was used in the calculation.

the TSA is largest in the troposphere (1.0–8.0%). The computation of the direct beam is identical in the TSA and DISORT. Hence, any difference between the results from the two arises from differences in the diffuse radiation. The increasing error with decreasing altitude is thus due to the increasing importance of multiple scattering as the atmosphere gets denser. Also the error increases with increasing solar zenith angle. This is due to larger optical pathlengths for larger solar zenith angles where multiple scattering becomes more important. When the surface albedo is zero the TSA underestimate both $J(O_3^*)$ and $J(O_3)$ for all altitudes and zenith angles, Figures 7a and 8a. For nonzero surface albedos (Figures 7b–7d and 8b–8d), the magnitude of the error decreases and becomes positive for high altitudes. This implies that the TSA overestimate the radiation reflected off the surface and underestimates the multiply scattered radiation. For the conditions considered here, the magnitude of the error made by the TSA for a Rayleigh scattering atmosphere for the $J(O_3)$ and $J(O_3)$ rates is never larger than the combined uncertainties for the appropriate cross sections and quantum yields (Table VI).

In Figures 9–10, we show results pertaining to a cloudy atmosphere. Photodissociation in the $J(O_3^*)$ channel is overestimated by the TSA below and inside the cloud and underestimated above the cloud for most albedos and solar zenith angles (Figure 9). The error increases with increasing surface albedo and may be as large as 60% below the cloud. However, in the stratosphere (15.0–50.0 km in the model atmosphere used here) the error is negligible. For the $J(O_3)$ channel (Figure 10) the situation is somewhat similar to the clear Rayleigh scattering atmosphere (Fig-
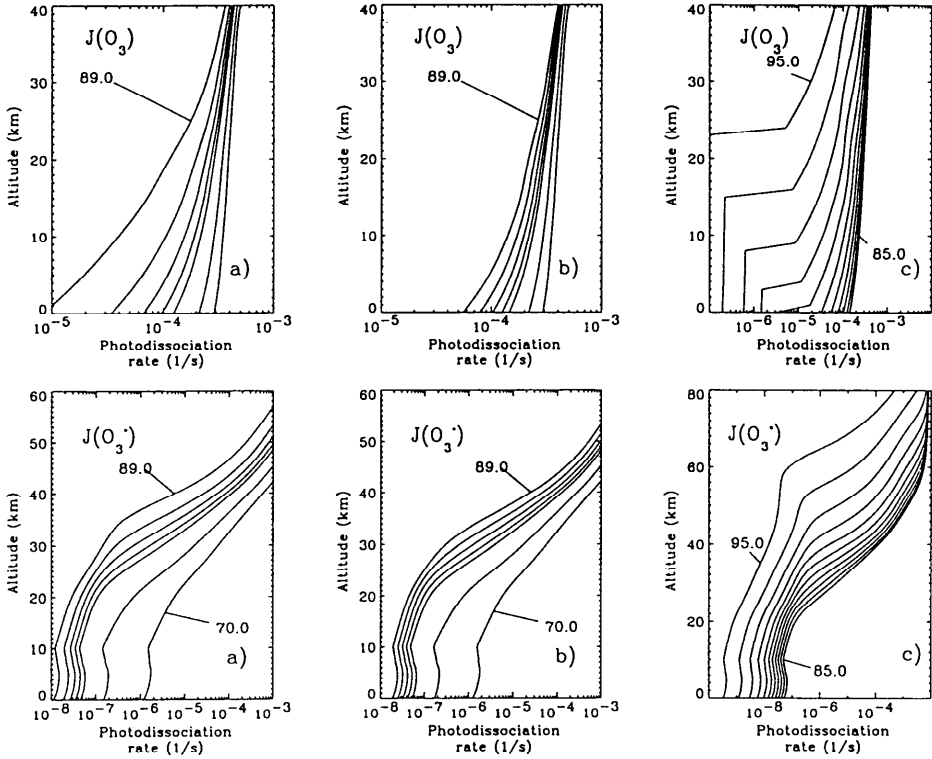
Fig. 5. The photodissociation rates $J(O_3)$: $O_3 + h\nu \rightarrow O(^1D) + O_2$ and $J(O_3^*)$: $O_3 + h\nu \rightarrow O(^3P) + O_2$ (lower panel) for different zenith angles and plane parallel and spherical geometry. (a) Shows the photodissociation rates calculated in plane-parallel geometry for solar zenith angles of 70, 80, 85, 86, 87, 88 and 89 degrees. (b) Shows the same rates in spherical geometry. Finally in (c) we show results for angles between 85° and 95° in 1° steps using spherical geometry. The relevant cross sections and quantum yields for the different reactions are from DeMore et al. (1990) and references therein. For the O_2 Schumann-Runge bands the parameterization of Allen and Frederick (1982) was used. The subarctic summer atmosphere (Anderson et al., 1987) and a surface albedo $A_g = 0.0$ was used in the calculation. Note the different scale on the y-axis in the panels.

$J(O_3^*)$ rate is less sensitive to changes in surface albedo or cloudiness than the $J(O_3)$ channel which is produced by radiation with wavelength longer than 310 nm. The presence of aerosols leads to increased scattering in the atmosphere. This can either lead to an increase or decrease in radiation depending on the change in the single scattering albedo, solar zenith angle and surface albedo. For the situation in Figure 6 the $J(O_3)$ photodissociation rate increases while the $J(O_3^*)$ rate decreases.

In Figures 7–12, we show the percentage error between the TSA results and the 16-stream computations. The clear sky results are shown in Figures 7–8. Both for the $J(O_3^*)$ rate (Figure 7), and the $J(O_3)$ rate (Figure 8), the error made by
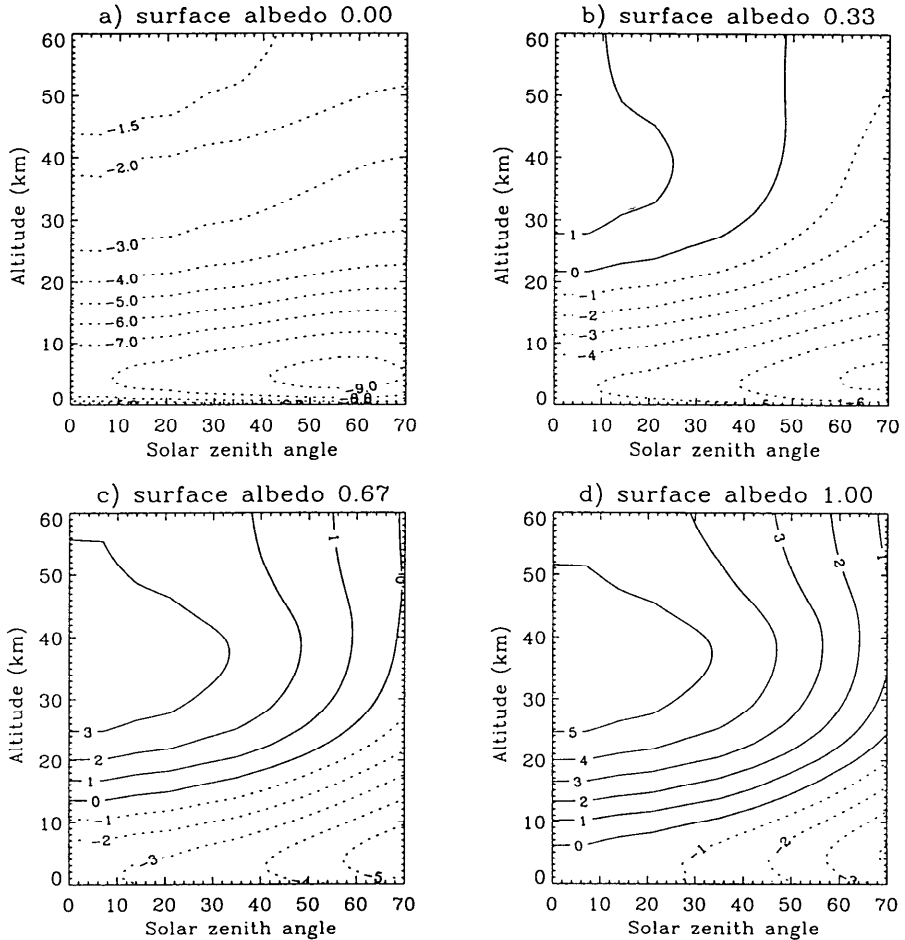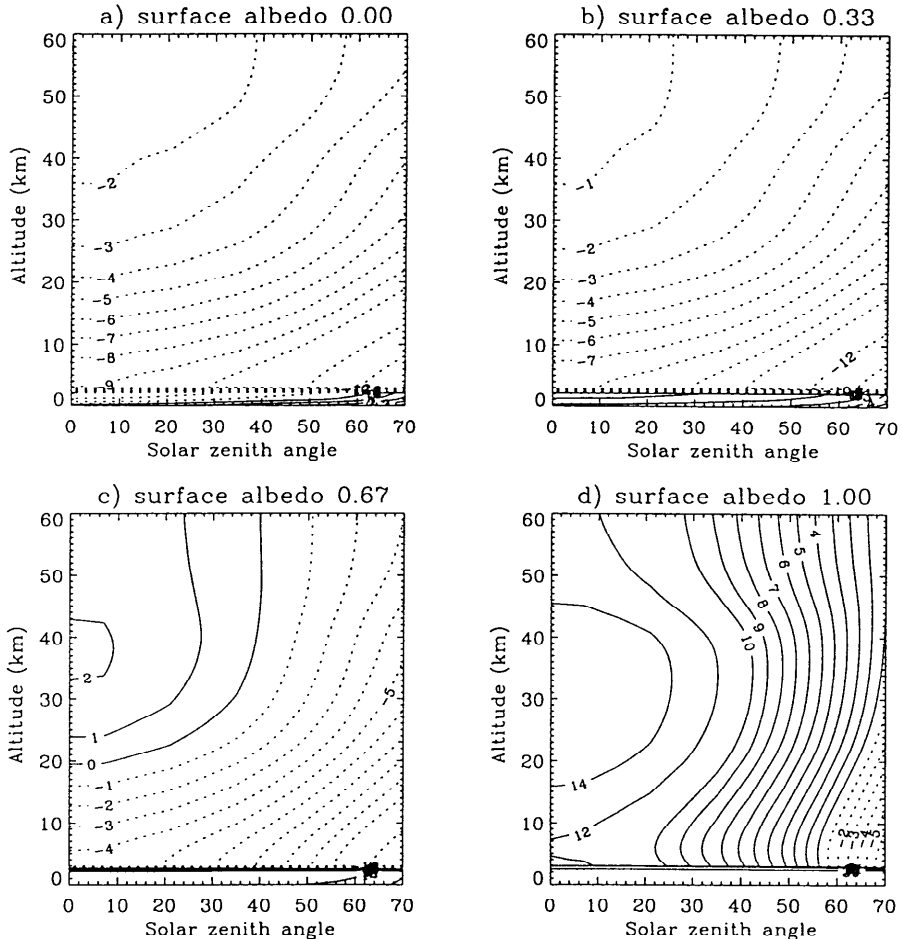
Fig. 8.   As in Figure 7, but for the $O_3 + h\nu \rightarrow O(^3P) + O_2$ photodissociation rate. Note different scale on y-axis in Figures 7–12.

ure 8). However, the error is larger and for large surface albedo values, the TSA may underestimate the $J(O_3)$ rate by up to 14% in the stratosphere. For more normal situations, i.e. lower surface albedos, the error is 2.0–8.0%. Below the cloud the TSA is larger by about 30% for large surface albedos, but less than 3.0–8.0% for more typical situations. Hence for certain albedos and altitudes the error made by the TSA in the calculation of $J(O_3)$ and $J(O_3^*)$ for a cloudy atmosphere may be as large or larger than the combined uncertainties for the appropriate cross sections and quantum yields (Table VI).

The error made by the TSA for an aerosol-loaded atmosphere is shown in Figures 11–12. The $J(O_3^*)$ channel is underestimated by the TSA in the troposphere. For small to moderate surface albedos (Figures 11a–b). For large surface albedos the
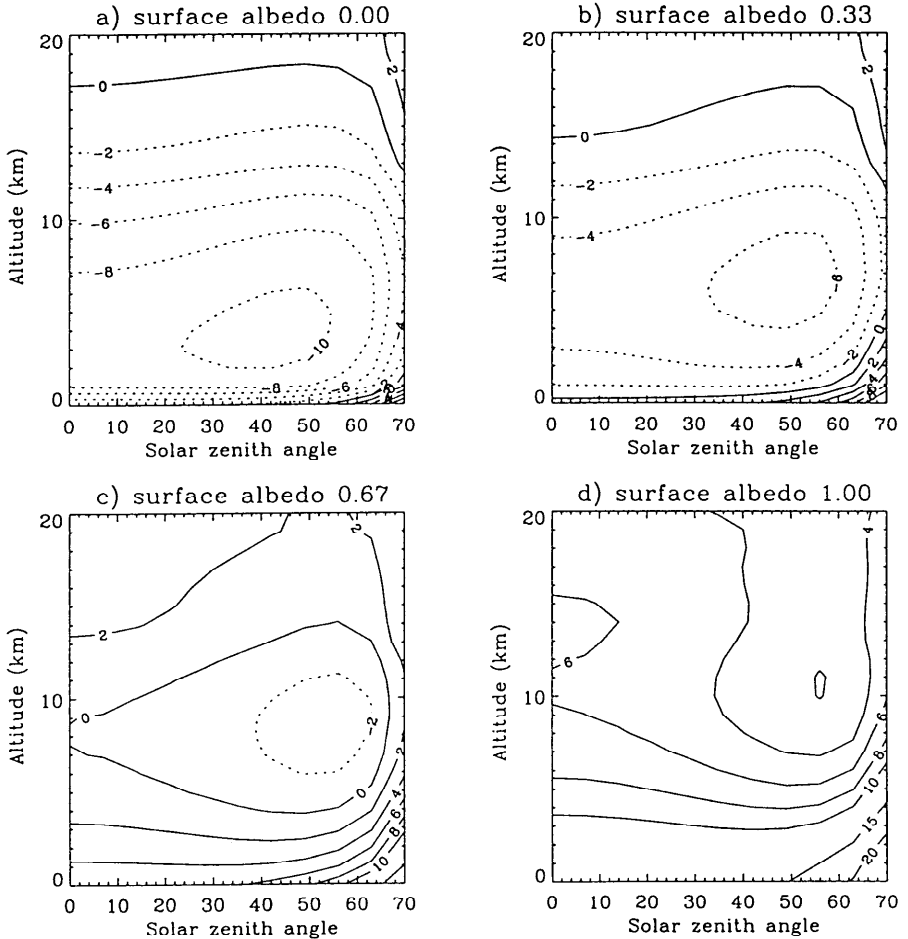
Fig. 7.   The percentage error $100 \times (J^2 - J^{16})/J^{16}$ for the $O_3 + h\nu \rightarrow O(^1D) + O_2$ photodissociation rate as a function of altitude and solar zenith angle for a clear Rayleigh scattering atmosphere. J^n is the photodissociation rate from an n-stream calculation. A midlatitude summer atmosphere (Anderson *et al.*, 1987) was used in the calculation. Negative errors are plotted with dottes lines and positive errors with solid lines. Note different scale on y-axis in Figures 7–12.

TABLE   VI. The photochemical reactions shown in Figure 5. The uncertainties shown represent the combined uncertainty for cross sections and quantum yields. They are not rigorous numbers, but qualitative estimates (DeMore *et al.*, 1992)

| Rate coefficient	Reaction	Uncertainty (%)
$J(O_3)$	$O_3 + h\nu \rightarrow O(^3P) + O_2$	10.0
$J(O_3^*)$	$O_3 + h\nu \rightarrow O(^1D) + O_2$	20.0

Fig. 10.   As in Figure 7, but for the $O_3 + h\nu \rightarrow O(^3P) + O_2$ photodissociation rate and a cloudy atmosphere. Note different scale on y-axis in Figures 7–12.

Here we estimate the error made by using the TSA as compared with more accurate multi-stream calculations. Ultraviolet (UV-B: 280–320 nm and UV-A: 320–400 nm) and visible (photosynthetically active radiation, PAR, 400–700 nm) fluxes are obtained by integrating the downward flux over wavelength (cf. Equation (17)). To assess the accuracy of the TSA for computing downward fluxes we compare two-stream and multi-stream results for UV-A, UV-B and PAR fluxes using the same clear, aerosol-loaded and cloudy atmospheres that we considered for the pho-todissociation rates. Note, however, that here the surface albedo was taken to be $A_g = 0.0, 0.1, 0.2, \ldots , 1.0$ and the solar zenith angle was increased in steps of $10°$ from $0°$ to $70°$. Furthermore, the wavelength resolution is 1.0 nm. The uvspec program of Kylling (1994) was used to compute the downward fluxes. The doses
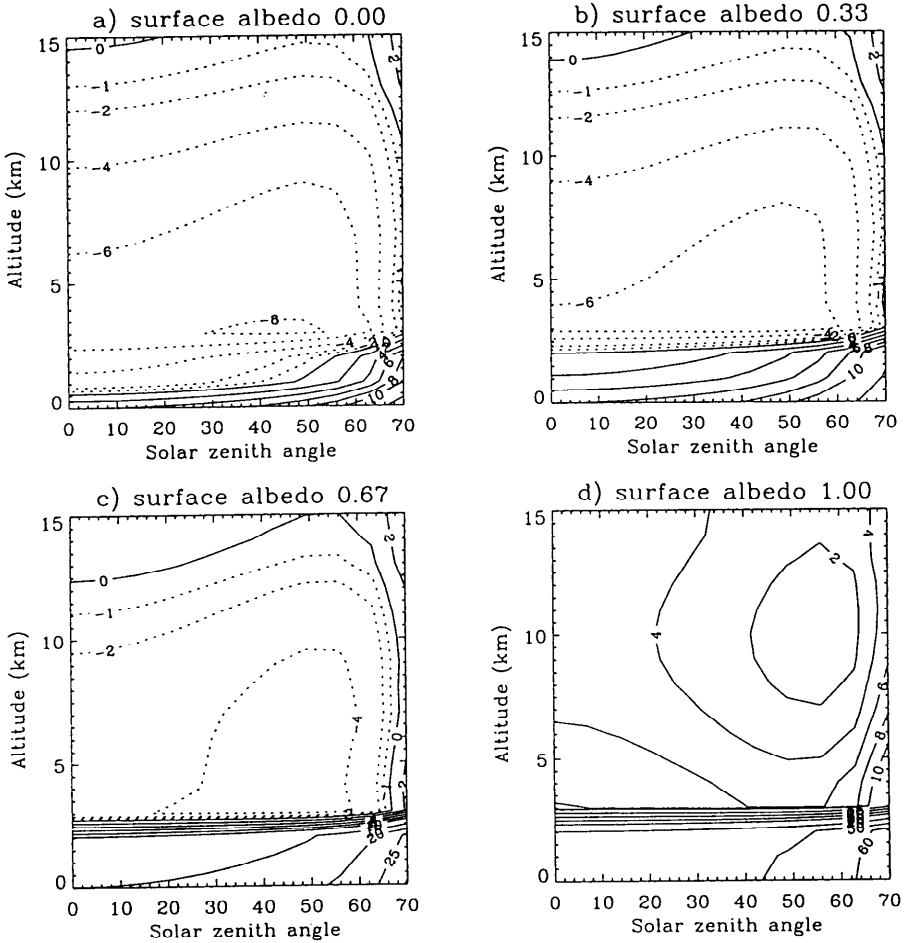
Fig. 9.   As in Figure 7, but for a cloudy atmosphere. Note different scale on y-axis in Figures 7–12.

TSA overestimates the $J(O_3^*)$ channel (Figures 11c–d). The error may be as large as 20%. Above the aerosol layer the error made by the TSA is small ($< 1.0\%$). The results for the $J(O_3)$ channel is displayed in Figure 12. For large solar zenith angles the TSA underestimates $J(O_3)$ by as much as 12% below the peak of the aerosol layer. The error decreases with increasing surface albedo. Above the aerosol layer the error may be up to 9% for large surface albedos.

4.6.   ULTRAVIOLET AND VISIBLE FLUXES: 2-STREAM VERSUS MULTI-STREAM RESULTS

Several investigators have used different two-stream approximations to study surface ultraviolet fluxes, e.g. Frederick and Lubin (1988), Brühl and Crutzen (1989).
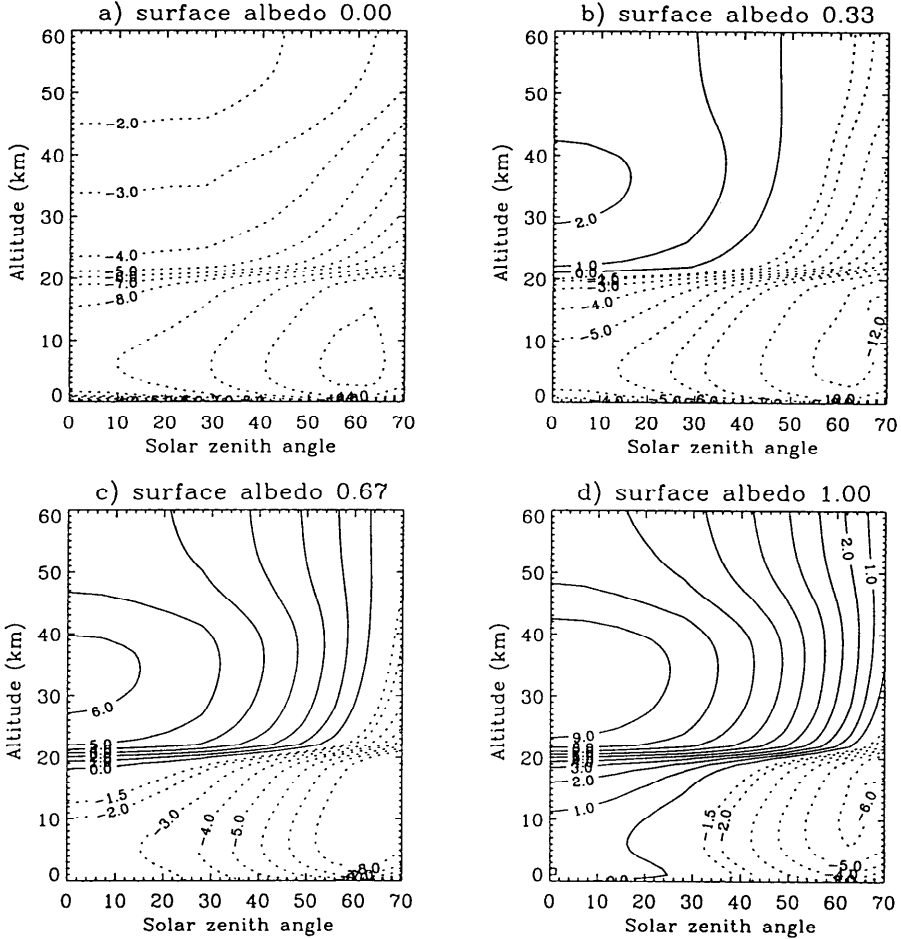
Fig. 12. As in Figure 7, but for the $O_3 + h\nu \rightarrow O(^3P) + O_2$ photodissociation rate and an aerosol loaded atmosphere. Note different scale on y-axis in Figures 7–12.

Here $\gamma(\mu_0)$ is the transmissivity of the atmosphere for $A_g = 0.0$ and ρ_s^* the spherical albedo for illumination from below. For a cloudy atmosphere ρ_s^* becomes large and gives the non-linear behavior of the fluxes as a function of the albedo as shown in Figure 13.

The percentage difference between the TSA and the accurate multi-stream computations are shown in Figure 14 as a function of the solar zenith angle and the surface albedo. Generally, the error made by the TSA increases with increasing surface albedo and solar zenith angle, i.e. the error increases with increasing photon pathlengths. As noted above, the difference between the TSA and the accurate multi-stream results are due to differences in the diffuse radiation. Hence, when pathlengths gets longer and multiple scattering becomes more important, the dif-
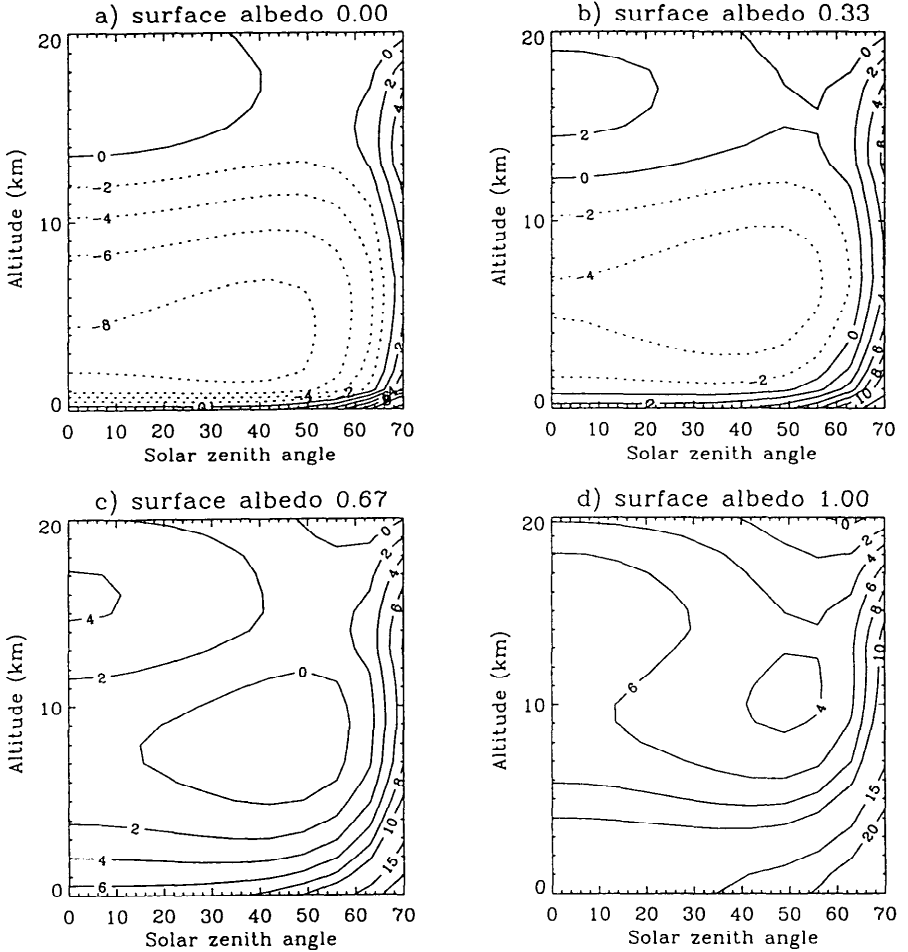
Fig. 11.   As in Figure 7, but for an aerosol loaded atmosphere. Note different scale on y-axis in Figures 7–12.

are computed from Equation (17) with the action spectrum taken to be $A(\lambda) = 1.0$ for simplicity. The rates are instantaneous rates, i.e., they have not been integrated over the day.

In Figure 13 we show UV-B, UV-A and PAR fluxes for a clear, cloudy and aerosol-loaded atmosphere as a function of surface albedo. The shape of the curves may be explained by noting that the transmittance of the atmosphere, $\gamma_A(\mu_0)$, may be written (Stamnes, 1982)

$$\gamma_A(\mu_0) = \gamma(\mu_0) + \frac{A_g \rho_s^*}{1 - A_g \rho_s^*} \gamma(\mu_0).$$

(18)
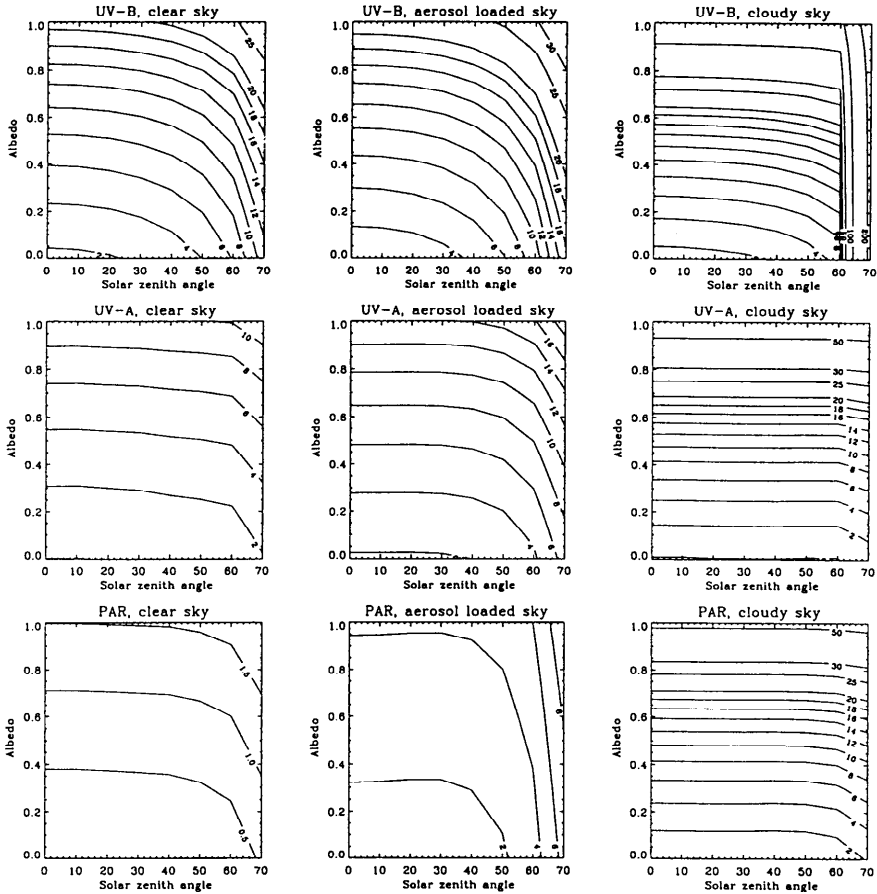
Fig. 14. The percentage difference between the TSA and the accurate multi-stream calculations for UV-B (upper panel), UV-A (middle panel) and PAR (lower panel). Results for clear (first column), aerosol-loaded (second column) and cloudy (third column) atmospheres are displayed as functions of the solar zenith angle and the surface albedo. Negative errors are plotted with dotted lines and positive errors with solid lines.

absorption by ozone, oxygen and nitrogen dioxide was included and the wavelength resolution was the same as for the calculation of the photodissociation rates. Both the warming and cooling rates were computed from Equation (16). The terrestrial cooling rates were computed with a quadrature angle $\mu_1 = 1/2$. Computations performed with $\mu_1 = 1/\sqrt{3}$ exhibited larger errors.

The warming/cooling rates for a clear, cloudy and aerosol-loaded atmosphere are shown in Figure 15. The difference between the TSA and the accurate multi-stream computations is displayed in Figure 16. The error in the warming rate is small for the clear and the cloudy atmosphere (Figure 16b). For the aerosol-loaded atmosphere the TSA underestimates the warming rate by 1.0 K/day at the altitude
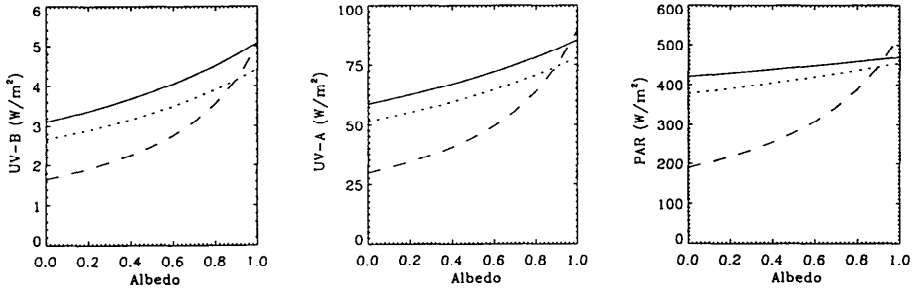
Fig. 13.   UV-B, UV-A and PAR as a function of the surface albedo for a clear Rayleigh scattering (solid line), aerosol-loaded (dotted line) and a cloudy (dashed line) atmosphere. The solar zenith angle is 30° and it is the accurate multi-stream results that are displayed.

TABLE VII. Upper limits for the solar zenith angle, θ_0, and the surface albedo, A_g, if 10.0% or less difference between the TSA and the accurate multi-stream results is to be achieved

UV-B, clear sky	$A_g < 0.65$ and $\theta_0 < 68.0$
UV-B, aerosol loaded sky	$A_g < 0.5$ and $\theta_0 < 64.0$
UV-B, cloudy sky	$A_g < 0.42$ and $\theta_0 < 58.0$
UV-A, clear sky	$A_g < 0.95$ or $\theta_0 < 60.0$
UV-A, aerosol loaded sky	$A_g < 0.62$
UV-A, cloudy sky	$A_g < 0.48$
PAR, clear sky	–
PAR, aerosol loaded sky	–
PAR, cloudy sky	$A_g < 0.48$

ference between the TSA and the multi-stream results increases. As can be seen from Figure 14, the error made by the TSA can be substantial for UV-B, UV-A and PAR fluxes for clear, cloudy and aerosol loaded atmospheres. If an error of 10.0% in downward fluxes is acceptable, the upper limits for the solar zenith angle and the surface albedo that give errors ≤ 10.0% are as listed in Table VII. Care should be exersized when using the TSA to compute downward fluxes for solar zenith angles greater than 60.0° or surface albedos greater than 0.5.

4.7. WARMING/COOLING RATES: 2-STREAM VERSUS MULTI-STREAM RESULTS

To estimate the accuracy of the TSA in realistic applications for thermal sources we computed atmospheric cooling rates for the same clear, aerosol-loaded and cloudy atmospheric situations as considered above. We also computed warming rates to demonstrate the error incurred by using the TSA. The cooling rates are computed using the correlated-k distribution method (Lacis and Oinas, 1991). Absorption by carbon dioxide, ozone and water molecules is accounted for. For the warming rate,

5. Summary

We have described a robust and reliable two-stream algorithm for radiative transfer computations, including multiple scattering, in vertically inhomogeneous pseudo-spherical media. This two-stream algorithm is essentially a 'stripped-down' version of the multi-stream (DISORT) algorithm (Stamnes *et al.*, 1988) and therefore contains all the advanced features of this unconditionally stable algorithm. However, it also contains the following new and unique features:

  (1) It includes the effect of spherical geometry, both in the direct and the diffuse radiation.
  (2) It includes an exponential-linear-in-depth approximation to the internal source allowing for efficient treatment of sources that vary rapidly with depth.

We have used this two-stream algorithm to investigate the accuracy of the two-stream approximation (TSA) in vertically inhomogeneous atmospheres, by computing photodissociation and warming/cooling rates and surface ultraviolet and visible fluxes for clear, cloudy and aerosol-loaded atmospheres. The two-stream results have been compared with accurate multi-stream computations. The $O_3 + h\nu \rightarrow O(^1D) + O_2$ and $O_3 + h\nu \rightarrow O(^3P) + O_2$ photodissociation rates were considered for solar zenith angles between 0.0–70.0° and surface albedos in the range 0.0–1.0. For small and moderate values of the solar zenith angle and the surface albedo the error made by the TSA is generally smaller, $< 10.0\%$, than the combined uncertainty in cross sections and quantum yields. Surface ultraviolet and visible fluxes were calculated for the same range of solar zenith angles and surface albedos as the photodissociation rates. It was found that surface ultraviolet and visible fluxes may be calculated by the TSA with 10% or less error for solar zenith angles less than 60.0° and surface albedos less than 0.5. For large solar zenith angles and/or large surface albedos, typical conditions at high latitudes, the error made by the TSA may become appreciable, i.e. 20% or more for the photodissociation rates in the lower stratosphere and for ultraviolet and visible surface fluxes for large surface albedos. The TSA agrees well with multi-stream results for computation of warming/cooling rates except for layers containing scattering matter where errors up to 10% may occur.

Finally it is noted that the general form of the internal source, cf. Equation (22), makes the present algorithm suitable for solving particle transport problems, as demonstrated by Stamnes *et al.* (1991).

Copies of the FORTRAN77 program are available by anonymous ftp to climate.gsfc.nasa.gov or else on floppy disk (IBM or Macintosh) from the third author.
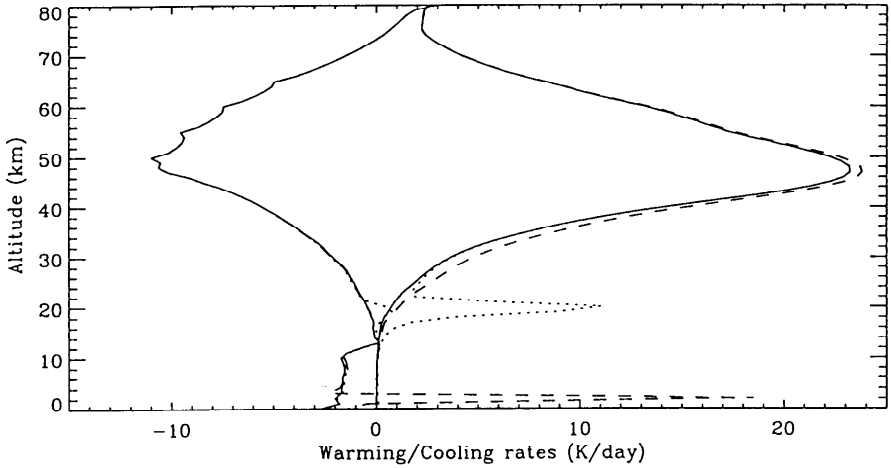
Fig. 15.   The solar and terrestrial warming/cooling rates for a clear (solid line), cloudy (dashed line) and aerosol-loaded (dotted line) atmosphere. All warming/cooling rates shown are instantaneous rates, i.e. they are not averaged over the day. The solar zenith angle is 35° and the surface albedo A_g=0.0. It is the accurate multi-stream results that are displayed.
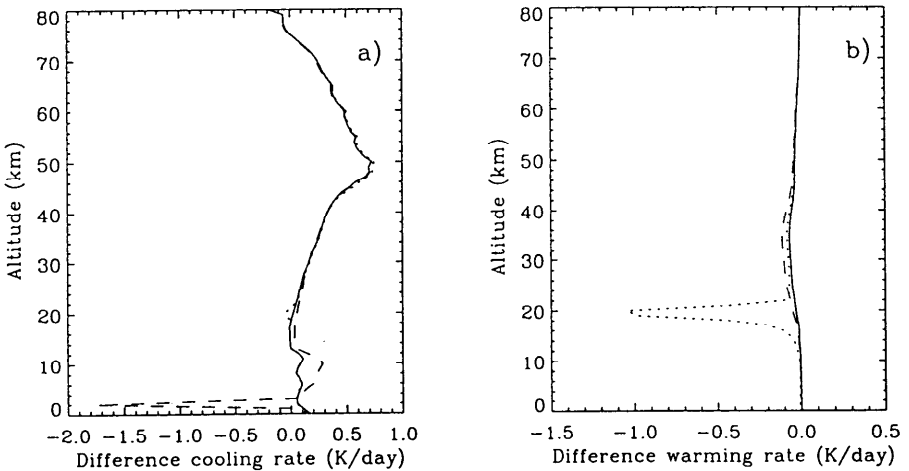
Fig. 16.   The difference between the TSA and the accurate multi-stream calculations for (a) the terrestrial and (b) the solar part of the spectrum. Results for clear (solid line), cloudy (dashed line) and aerosol-loaded (dotted line) atmospheres are shown.

where the maximum aerosol concentration is. The cooling rate is accurate to less than 0.7 K/day at all altitudes and for all three atmospheric conditions except inside the cloud for the cloudy atmosphere where the TSA underestimates the cooling by 1.8 K/day which is about 10% lower than the value obtained by the 16-stream calculation.

we get after insertion of Equation (23) into Equations (7)–(8), and equating coefficients of like powers of τ

$$Y_1^\pm = \frac{abX_1^\mp + (1 - a + ab \mp \alpha\mu_1)X_1^\pm}{(1 - a)(1 - a + 2ab) - (\alpha\mu_1)^2}, \tag{24}$$

$$Y_0^\pm = \frac{abZ_0^\mp + (1 - a + ab \mp \alpha\mu_1)Z_0^\pm}{(1 - a)(1 - a + 2ab) - (\alpha\mu_1)^2}, \tag{25}$$

where

$$Z_0^\pm = X_0^\pm \pm \mu_1 Y_1^\pm. \tag{26}$$

We may thus write the full solution to Equation (1) for layer p as

$$I_p^\pm(\tau) = C_p^- g_p^-(\pm\mu_1)e^{k_p\tau} + C_p^+ g_p^+(\pm\mu_1)e^{-k_p\tau} + $$
$$+ e^{-\alpha_p^b\tau}(Y_{b0,\,p}^\pm + Y_{b1,\,p}^\pm\tau) + e^{-\alpha_p^P\tau}(Y_{P0,\,p}^\pm + Y_{P1,\,p}^\pm\tau), \tag{27}$$

where the b superscript stands for the direct beam pseudo source and P for the internal thermal source.

A.3. BOUNDARY CONDITIONS

We allow the medium to be illuminated from above by known uniform incidence of particles or radiation (incident parallel beams are treated as pseudo sources)

$$I_1^-(\tau = 0) = F^s. \tag{28}$$

Furthermore, across layer interfaces we require the intensities to be continuous

$$I_p^\pm(\tau_p) = I_{p+1}^\pm(\tau_p), \qquad p = 1, \ldots, L - 1. \tag{29}$$

Finally, the medium may be forced by uniform incidence at the bottom boundary due to Lambertian reflection and/or emission of particles or radiation. If the bottom boundary has temperature T_g, emissivity ϵ and behaves as a Lambertian reflector with albedo A_g, then

$$I_L^+(\tau_L) = I^g = 2A_g\mu_1 I_L^-(\tau_L) + \epsilon B[T_g]. \tag{30}$$

A.4. SCALING TRANSFORMATION

Insertion of Equation (27) into Equations (28–(30) would give us a complete set of linear algebraic equations to solve for the constants of integration $C_p^\pm$. However, to avoid 'catastrophic' numerical ill-conditioning, it is necessary to remove the positive exponentials in Equation (27). This is achieved by the scaling transformation (Stamnes and Conklin, 1984)

$$C_p^+ = \tilde{C}_p^+ e^{k_p\tau_p - 1}, \tag{31}$$

$$C_p^- = \tilde{C}_p^- e^{-k_p \tau_p}. \tag{32}$$

Insertion of Equation (27) into Equations (28)–(30) using Equations (31)–(32) yields

$$\tilde{C}_1^- D_1 e^{-k_1 \tau_1} + \tilde{C}_1^+ = F^s - R_1^-(0), \tag{33}$$

$$\tilde{C}_p^- D_p + \tilde{C}_p^+ e^{-k_p(\tau_p - \tau_{p-1})} - \tilde{C}_{p+1}^- D_{p+1} e^{-k_{p+1}(\tau_{p+1} - \tau_p)} - \tilde{C}_{p+1}^+$$
$$= R_{p+1}^-(\tau_p) - R_p^-(\tau_p), \tag{34}$$

$$\tilde{C}_p^- + \tilde{C}_p^+ D_p e^{-k_p(\tau_p - \tau_{p-1})} - \tilde{C}_{p+1}^- e^{-k_{p+1}(\tau_{p+1} - \tau_p)} - \tilde{C}_{p+1}^+ D_{p+1}$$
$$= R_{p+1}^+(\tau_p) - R_p^+(\tau_p), \qquad p = 1, \dots, L - 1 \tag{35}$$

$$\tilde{C}_L^-(1 - 2A_g\mu_1 D_L) + \tilde{C}_L^+(D_L - 2A_g\mu_1) e^{-k_L(\tau_L - \tau_{L-1})}$$
$$= 2A_g\mu_1 R_L^-(\tau_L) - R_L^+(\tau_L) + \epsilon_g B[T_g], \tag{36}$$

where

$$R_p^\pm(\tau) = R_p(\tau, \pm\mu_1) = e^{-\alpha_p^b \tau}(Y_{b0,\,p}^\pm + Y_{b1,\,p}^\pm \tau) + $$
$$+ e^{-\alpha_p^P \tau}(Y_{P0,\,p}^\pm + Y_{P1,\,p}^\pm \tau). \tag{37}$$

Equations (33)–(36) constitute a $(2 \times L) \times (2 \times L)$ system of linear algebraic equations from which the $2 \times L$ unknown coefficients $C_p^\pm$ ($p = 1, \dots, L$) are determined. The coefficient matrix is pentadiagonal and may be inverted by special routines for banded matrices, e.g. LINPACK (Dongerra et al., 1979). The speed of solving this pentadiagonal system is linear in L, the number of layers (Stamnes and Conklin, 1984). As pointed out by Toon et al. (1989), Equations (33)–(36) may be rewritten in tridiagonal form as follows:

$$\tilde{C}_1^- D_1 e^{-k_1 \tau_1} + \tilde{C}_1^+ = F^s - R_1^-(0), \tag{38}$$

$$(1 - D_p D_{p+1})\tilde{C}_p^- + (D_p - D_{p+1}) e^{-k_p(\tau_p - \tau_{p-1})}\tilde{C}_p^+ -$$
$$- (1 - D_{p+1}^2) e^{-k_{p+1}(\tau_{p+1} - \tau_p)}\tilde{C}_{p+1}^-$$
$$= R_{p+1}^+(\tau_p) - R_p^+(\tau_p) - D_{p+1}(R_{p+1}^-(\tau_p) - R_p^-(\tau_p)), \tag{39}$$

$$(1 - D_p^2)e^{-k_p(\tau_p - \tau_{p-1})}\tilde{C}_p^+ + (D_p - D_{p+1}) e^{-k_{p+1}(\tau_{p+1} - \tau_p)}\tilde{C}_{p+1}^- -$$
$$- (1 - D_p D_{p+1})\tilde{C}_{p+1}^+$$
$$= R_{p+1}^-(\tau_p) - R_p^-(\tau_p) - D_p(R_{p+1}^+(\tau_p) - R_p^+(\tau_p)), \tag{40}$$
$$p = 1, \dots, L - 1,$$

$$\tilde{C}_L^-(1 - 2A_g\mu_1 D_L) + \tilde{C}_L^+(D_L - 2A_g\mu_1)e^{-k_L(\tau_L - \tau_{L-1})}$$

$$= 2A_g\mu_1 R_L^-(\tau_L) - R_L^+(\tau_L) + \epsilon_g B[T_g]. \tag{41}$$

The computer time needed to solve this tridiagonal matrix is still linear in L and is thus in principle not any faster than solving the pentadiagonal matrix. However, tridiagonal solvers (Vetterling et al., 1985) are compact and significant computing efficiency may be lost in more general solvers due to 'overhead' operations. Generally, pivoting is not incorporated into tridiagonal solvers. During the test phase of the present two-stream method with the 'tridag' tridiagonal solver (Vetterling et al., 1985) we encountered several cases where tridag 'broke down' resulting in erroneous radiative quantities. Running 'tridag' in double precision only partly cured the problem. Thus, pivoting should be included when solving for the constants of integration. To get both a fast and numerically stable code we thus use the LINPACK routines SGBCO and SGBSL to solve the tridiagonal matrix, (Equations (38)–(41)), in the present two-stream method. These LINPACK routines are designed to solve a general banded matrix and include pivoting. Vectorized versions of these routines are also available and may be of interest to users with 'vector machines'.

A.5. SCALED SOLUTION

Finally, by incorporating the scaling into the homogeneous solution the intensity in the directions $\pm\mu_1$ may be written as

$$I_p^-(\tau) = \tilde{C}_p^- D_p\, e^{-k_p(\tau - \tau)} + \tilde{C}_p^+\, e^{-k_p(\tau - \tau_{p-1})} + R_p(\tau, -\mu_1), \tag{42}$$

$$I_p^+(\tau) = \tilde{C}_p^-\, e^{-k_p(\tau_p - \tau)} + \tilde{C}_p^+ D_p\, e^{-k_p(\tau - \tau_{p-1})} + R_p(\tau, +\mu_1). \tag{43}$$

We note that the arguments of the exponentials in the scaled solutions are now negative implying that numerical overflow is avoided in the computation. It should also be noted that Equation (42)–(43) allows us to compute the radiation field at any optical depth in the medium, since similar analytic solutions exist for all layers.

Appendix B. The Chapman Function

The Chapman function for zenith angles $\theta_0 \leq 90°$ is given by (e.g. Rees, 1989)

$$\mathrm{ch}(z_0,\ \theta_0) = \sum_j \sigma_j \int_{z_0}^{\infty} n_j(z)\frac{\mathrm{d}z}{\sqrt{1 - \left(\frac{R+z_0}{R+z}\right)^2 \sin^2\theta_0}} \tag{44}$$

and for zenith angles greater than $90°$ by

$$\mathrm{ch}(z_0,\ \theta_0) =$$

$$= \sum_j \sigma_j \left\{ 2\int_{z_s}^{\infty} n_j(z)\frac{\mathrm{d}z}{\sqrt{1 - \left(\frac{R+z_s}{R+z}\right)^2}} - \int_{z_0}^{\infty} n_j(z)\frac{\mathrm{d}z}{\sqrt{1 - \left(\frac{R+z_0}{R+z}\right)^2 \sin^2\theta_0}} \right\}. \tag{45}$$
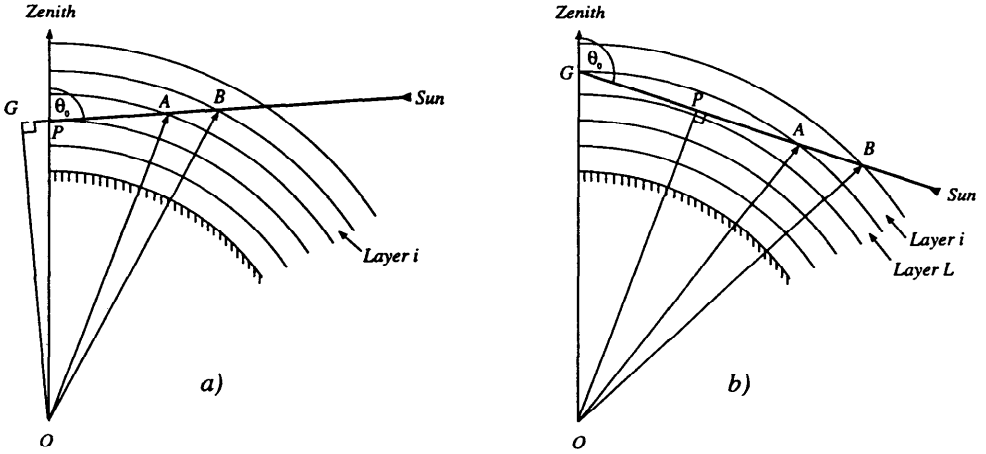
Fig. 17. Geometry for calculation of the Chapman function in a spherical layered atmosphere. In (a) for solar angles $\theta_0 \leq 90.0°$ and in (b) for solar zenith angles $\theta_0 > 90.0°$.

Here $n_j(z)$ is the number density of the j'th species and σ_j the corresponding cross section. The radius of the planet in question is denoted by R, z_s is the screening height and z_0 the height at which the optical depth is desired. The above integrals may generally not be evaluated analytically. We use the approach of Dahlback and Stamnes (1991) in which the plane-parallel optical depth of each layer $\Delta\tau_i$ is modified by a geometric correction factor $\Delta s_i/\Delta h_i$. With reference to Figure 17 the thickness of each layer $\Delta h_i = r_i - r_{i+1}$, where $r_{i+1} = $ OA and $r_i = $ OB. Furthermore, $\Delta s_i = $ AB $ = $ GB $ - $ GA $ = \sqrt{r_i^2 - r_p^2 \sin^2 \theta_0} - \sqrt{r_{i+1}^2 - r_p^2 \sin^2 \theta_0}$, since OG $ = r_p^2 \sin^2 \theta_0$ and $r_p = $ OP. Thus for $\theta_0 \leq 90°$ we have

$$\mathrm{ch}(z_0, \ \theta_0) = \sum_{i=1}^{p} \Delta\tau_i \frac{\Delta s_i}{\Delta h_i} \ , \tag{46}$$

and for $\theta_0 > 90°$

$$\mathrm{ch}(z_0, \ \theta_0) = \sum_{i=1}^{p} \Delta\tau_i \frac{\Delta s_i}{\Delta h_i} + 2 \sum_{i=p+1}^{L} \Delta\tau_i \frac{\Delta s_i}{\Delta h_i} + \Delta\tau_L \frac{\Delta s_L}{\Delta h_L} \ , \tag{47}$$

where L is the deepest layer in the atmosphere for which the attenuated direct beam is non-negligible. We have compared this simple evaluation of the Chapman function with more elaborate evaluations of the integrals in Equations (44)–(45). For a variety of zenith angles between 80° and 95° and for different optical thicknesses excellent agreement was found (L- Perliski and S. Solomon, 1991, private communication).

References

1. Allen, M. and Frederick, J. E., 1982, Effective photodissociation cross sections for molecular oxygen and nitric oxide in the Schumann-Runge bands, *J. Atmos. Sci.* **39**, 2066.
2. Anderson, G. P., Clough, S. A., Kneizys, F. X., Chetwynd, J. H., and Shettle, E. P., 1987, AFGL Atmospheric Constituent Profiles (0–120 km), AFGL-TR-86-0110, AFGL (OPI), Hanscom AFB, MA 01736.
3. Bohren, C. F., 1987, Multiple scattering of light and some of its observable consequences, *American J. Phys.* **55**, 524–533.
4. Brühl, C. and Crutzen, P. J., 1989, On the disproportionate role of tropospheric ozone as a filter against solar UV-B radiation, *Geophys. Res. Lett.* **16**, 703–706.
5. Chandrasekhar, S., 1960, *Radiative Transfer* (Dover, New York).
6. Dahlback, A., Henriksen, T., Larsen, S. H. H., and Stamnes, K., 1989, Biological UV-doses and the effect of an ozone layer depletion, *Photochemistry and Photobiology* **49**, 621.
7. Dahlback, A. and Stamnes, K., 1991, A new spherical model for computing the radiation field available for photolysis and heating at twilight, *Planet. Space Sci.* **39**, 671–683.
8. DeMore, W. B. *et al.*, 1992, Chemical kinetics and photochemical data for use in stratospheric modeling, Evaluation number 10, JPL publ. 92-20. Jet Propul. Lab., Pasadena, Calif.
9. Dongerra, J. J., Moler, C. B., Bunch, J. R., and Stewart, G. W., 1979, LINPACK *User's Guide*, (SIAM, Philadelphia).
10. Frederick, J. E. and Lubin, D., 1988, The budget of biologically active ultraviolet radiation in the Earth-Atmosphere system, *J. Geophys. Res.* **93**, 3825–3832.
11. Goody, R. M. and Yung, Y. L., 1989, *Atmospheric Radiation: Theoretical Basis*, Oxford University Press, New York.
12. Hansen, J. and Lacis, A. A., 1990, Sun and dust versus greenhouse gases: An assessment of their relative roles in global climate change, *Nature* **346**, 713–719.
13. Hu, Y. X. and Stamnes, K., 1993, An accurate parameterization of the radiative properties of water clouds suitable for use in climate models, *J. Clim.* **6**, 728–742.
14. Joseph, J., Wiscombe, W. J., and Weinman, J. A., 1976, The delta-Eddington approximation for radiative flux transfer, *J. Atmos. Sci.* **33**, 2452–2459.
15. King, M. D. and Harshvardhan, 1986, Comparative accuracy of selected multiple scattering approximations, *J. Atmos. Sci.* **43**, 784–801.
16. Kylling, A., 1992, Radiation transport in cloudy and aerosol loaded atmospheres, Ph.D. thesis, University of Alaska-Fairbanks.
17. Kylling, A. and Stamnes, K., 1992, Efficient yet accurate solution of the linear transport equation in the presence of internal sources: The exponential-linear approximation, *J. Comp. Phys.* **102**, 265–276.
18. Kylling, A., 1994, uvspec, a program for calculation of diffuse and direct uv and visible fluxes on horizontal surfaces, available by anonymous ftp to kaja.gi.alaska.edu, cd pub/arve.
19. Lacis, A., Oinas, A. and V., 1991, A description of the correlated *k* distribution method for modeling nongray gaseous absorption, thermal emission, and multiple scattering in vertically inhomogenous atmospheres, *J. Geophys. Res.* **96**, 9027–9063.

20. Lenoble, J., 1985, *Radiative Transfer in Scattering and Absorbing Atmospheres: Standard Computational Procedures*, A. Deepak, Hampton, Va.
21. Madronich, S., 1987, Photodissociation in the atmosphere: 1. Actinic flux and the effects of ground albedo and clouds, *J. Geophys. Res.* **92**, 9740–9752.
22. Madronich, S. and Weller, G., 1990, Numerical integration errors in calculated tropospheric photodissociation rate coefficients, *J. Atmos. Chem.* **10**, 289–300.
23. Meador, W. E. and Weaver, W. R., 1980, Two-stream approximations to radiative transfer in planetary atmospheres: A unified description of existing methods and new improvements, *J. Atmos. Sci.* **37**, 630–643.
24. Nagy, A. F. and Banks, P. M., 1970, Photoelectron fluxes in the ionosphere, *J. Geophys. Res.* **75**, 6260–6270.
25. Rees, M. H., *Physics and chemistry of the upper atmosphere* (Cambridge University Press, 1989).
26. Schaller, E., 1979, A delta-two-stream approximation in radiative flux calculations, *Contrib. Atmos. Phys.* **52**, 17–26.
27. Shettle, E. P., 1989, Models of aerosols, clouds and precipitation for atmospheric propagation studies, in AGARD Conference Proceedings No. 454, *Atmospheric propagation in the uv, visible, ir and mm-region and related system aspects*.
28. Stamnes, K., 1981, On the two-stream approach to electron transport and thermalization, *J. Geophys. Res.* **86**, 2408–2410.
29. Stamnes, K., 1982, Reflection and transmission by a vertically inhomogeneous planetary atmosphere, *Planet. Space Sci.* **30**, 727–732.
30. Stamnes, K. and Conklin, P., 1984, A new multi-layer discrete ordinate approach to radiative transfer in vertically inhomogeneous atmospheres, *J. Quant. Spectrosc. Radiat. Transfer* **31**, 273.
31. Stamnes, K., 1986, The theory of multiple scattering of radiation in plane-parallel atmospheres, *Rev. Geophys.* **24**, 299–310.
32. Stamnes, K., Tsay, S.-C., Wiscombe, W., and Jayaweera, K., 1988, Numerically stable algorithm for discrete-ordinate-method radiative transfer in multiple scattering and emitting layered media, *Applied Optics* **27**, 2502.
33. Stamnes, K., Lie-Svendsen, Ø., and Rees, M. H., 1991, The linear Boltzmann equation in slab geometry: Development and verification of a reliable and efficient solution, *Planet. Space Sci.* **39**, 1435–1463.
34. Toon, O. B., McKay, C. P., and Ackerman, T. P., 1989, Rapid calculation of radiative heating rates and photodissociation rates in inhomogeneous multiple scattering atmospheres, *J. Geophys. Res.* **94**, 16 287–16 301.
35. Turco, R. P., Whitten, R. C., and Toon, O. B., 1982, Stratospheric Aerosols: Observation and Theory, *J. Geophys. Res.* **20**, 233–279.
36. Vetterling, W. T., Teukolsky, S. A., Press, W. H., and Flannery, B. P., 1985, *Numerical Recipes: Example Book (FORTRAN)*, Cambridge University Press.
37. Wiscombe, W., 1977a, The delta-Eddington approximation for a vertically inhomogeneous atmosphere', NCAR Tech. Note NCAR/TN-121+STR.
38. Wiscombe, W., 1977b, The Delta-M method: Rapid yet accurate radiative flux calculations for strongly asymmetric phase functions, *J. Atmos. Sci.* **34**, 1408.
39. World Meteorological Organization, 1986, Atmospheric Ozone 1985, Assessment of our understanding of the processes controlling its present distribution and changes, *Rep. 16*, Global Ozone Res. and Monit. Proj., Geneva, Switzerland.
40. Zdunkowski, W., Welch, R., and Korb, G., 1980, An investigation of the structure of typical two-stream methods for the calculation of solar fluxes and heating rates in clouds, *Contribut. Atmos. Phys.* **53**, 147–165.